



UNIVERSITY OF THESSALY

DEPARTMENT OF ELECTRICAL AND COMPUTER
ENGINEERING

DIPLOMA THESIS

**SOLAR BUSINESS CASE ANALYZER: ROOFTOP DETECTION
AND PV PERFORMANCE PREDICTION**

Ioanna Emmanouilidou

Athanasios Tolis

Supervisors

Lefteri H. Tsoukalas, Professor

Michael Vassilakopoulos, Associate Professor

Volos, February 2019



UNIVERSITY OF THESSALY

DEPARTMENT OF ELECTRICAL AND COMPUTER
ENGINEERING

DIPLOMA THESIS

**SOLAR BUSINESS CASE ANALYZER: ROOFTOP DETECTION
AND PV PERFORMANCE PREDICTION**

Ioanna Emmanouilidou

Athanasios Tolis

Supervisors

Lefteri H. Tsoukalas, Professor

Michael Vassilakopoulos, Associate Professor

Volos, February 2019



ΠΑΝΕΠΙΣΤΗΜΙΟ ΘΕΣΣΑΛΙΑΣ
ΤΜΗΜΑ ΗΛΕΚΤΡΟΛΟΓΩΝ ΜΗΧΑΝΙΚΩΝ ΚΑΙ
ΜΗΧΑΝΙΚΩΝ ΥΠΟΛΟΓΙΣΤΩΝ

ΔΙΠΛΩΜΑΤΙΚΗ ΕΡΓΑΣΙΑ

**ΑΝΑΛΥΣΗ ΕΠΙΧΕΙΡΗΜΑΤΙΚΩΝ ΣΧΕΔΙΩΝ
ΦΩΤΟΒΟΛΤΑΙΚΩΝ ΕΦΑΡΜΟΓΩΝ: ΔΕΔΟΜΕΝΑ
ΕΓΚΑΤΑΣΤΑΣΕΩΝ ΚΑΙ ΕΚΤΙΜΗΣΗ ΑΠΟΔΟΣΗΣ**

Ιωάννα Εμμανουηλίδου
Αθανάσιος Τόλης

Επιβλέποντες Καθηγητές

Ελευθέριος Τσουκαλάς, Καθηγητής
Μιχαήλ Βασιλακόπουλος, Αναπληρωτής, Καθηγητής
Βόλος, Φεβρουάριος 2019

This page was intentionally left blank.

ACKNOWLEDGEMENTS

Reaching the final destination of this exciting journey of knowledge, it is my duty to recall all those people who contribute in their own unique ways in accomplishing my academic goals.

First and foremost, I would like to express my sincere acknowledgements to Professor Lefteri H. Tsoukalas, as well as to Associate Professor Michael Vassilakopoulos for undertaking the supervision of my thesis and for giving me their invaluable support and guidance throughout the whole process. I would also like to sincerely thank Emeritus professor Elias N. Houstis for inducting me in the extraordinary world of data through his courses. Furthermore, I would like to extend my sincere esteems to Associate Professor Dimitrios Bargiotas. His constructive comments were crucial for the completion of this work.

Moreover, I would like to express my heartfelt gratitude to my amazing friends, for standing by my side all this time. You brighten my academic years and I feel fortunate that I had the chance to meet each one of you. Most of all I want to thank my partner in crime Ioanna Emmanouilidou for sharing together this piece of work and being my life-coach for the last couple of months. Your enthusiasm and positivity, your persistent support and encouragement were vital. I will always be grateful for being a part of this journey.

Last but not least, I would like to thank my parents Electra and Nikos for their unconditional love and continuous support that made me the person I am today. I owe it all to you.

Athanasios Tolis
Arta, February 2019

A big journey is coming to an end, a long-lasting, bittersweet process which concludes with the completion of this Diploma Thesis. This endeavor would never be possible without the most crucial ingredient, the people in my life who stood by me, supported me in unfathomable ways and were my rocks, even when things were not ideal.

First of all, I would like to thank our professor, Elias Houstis, for his ongoing help and encouragement through this process and for offering me the chance through his courses to discover the fascinating world of data science. Furthermore, I would like to express my sincere appreciation to Professor Lefteri H. Tsoukalas, as well as to Associate Professor Michael Vassilakopoulos who supervised us during the past months and, with their knowledge, actively contributed to our research. Last but not least, my heartfelt appreciation goes to Associate Professor Dimitrios Bargiotas for his advice and constructive criticism, which helped our study in many ways.

All these years, my parents' and my sister's support and belief in me kept me going, motivated me and pushed me forward to take risks and do my best, knowing that my safety net would always be there to catch me if I fall. In addition, I will always be indebted to other members of my family, who always had my back and continuously expressed their unconditional love to me. I will never forget all the friends that were beside me, at the lowest of my lows and the highest of my highs, to celebrate with me in the good and uplift me in the bad times.

Furthermore, I would like to offer my sincerest thanks to the people in Amsterdam that offered me an internship that was bound to change my perspective for life: the light-bringers, the magic makers, the game shakers that challenged me and equipped me with more knowledge than I could imagine in such a short amount of time.

Last in order, but not of importance, words cannot describe the gratitude I feel for the unwavering support of my partner, Thanos, who uplifted me and was by my side, no matter what. This research, and my journey in knowledge, would not be possible without his contributions. A thank you will never be enough.

Ioanna Emmanouilidou
Amsterdam, February 2019

ABSTRACT

In the recent years, the changes in the domain of electricity production and consumption are constant and fast-moving. Paired with the harsh environmental impact and the depletion of fossil fuels, the need for a 180-turn to renewable energy sources arises stronger than ever. Despite being known for its windmills and green energy, the Netherlands are actually amongst the worst performers in the European Union, with only 7% of renewable energy share. The fact that the country will miss 2020 targets for renewable energy production and greenhouse gas emissions, paired with the replacement of the current net-metering scheme with a not particularly favorable return subsidy, highlight the need to research and study new opportunities focused on solar power systems. Even though the number of solar energy installations increases day to day, with the installed capacity overpassing 4 MW, a great number of Dutch people has not ventured towards that direction yet.

This thesis is going to describe the implementation of a solar business case analyzer, aimed to provide people with a free, easy way to assess the solar potential of buildings. As a first step, we implement rooftop detection on satellite images through the use of the Mask R-CNN computer vision algorithm. After benchmarking the results, the efficiency of this method is measured at an average of 77.94% for all building categories. Afterwards, by employing Python's pvlb library, we model the installation of a PV system and simulate the Return of Investment and earnings throughout a period of 10 years for a building in Hoofddorp. This study intends to create a generic framework that will be later used in the development of a web application, aiming to provide citizens with a tool to simplify their decisions regarding their solar energy system.

ΠΕΡΙΛΗΨΗ

Κατά τη διάρκεια των τελευταίων ετών, οι αλλαγές στην παραγωγή και την κατανάλωση της ηλεκτρικής ενέργειας είναι ολοένα και πιο ραγδαίες. Το γεγονός αυτό σε συνδυασμό με τις ολέθριες περιβαλλοντικές συνέπειες και την εξάντληση των ορυκτών καυσίμων αποτελεί ένα μεγάλο κίνητρο για στροφή 180 μοιρών προς τις ανανεώσιμες μορφές ενέργειας. Παρά τη φήμη της για τους ανεμόμυλους και την αιολική ενέργεια, η Ολλανδία στην πραγματικότητα βρίσκεται στις χαμηλότερες θέσεις των ‘πράσινων’ χωρών της Ευρωπαϊκής Ένωσης, καθώς μόλις 7% της κατανάλωσης ηλεκτρικής ενέργειας προέρχεται από ανανεώσιμες πηγές. Δεδομένου ότι οι στόχοι του 2020 που αφορούν την παραγωγή ανανεώσιμης ενέργειας και τη μείωση εκπομπών αερίων του θερμοκηπίου δε θα επιτευχθούν, ενώ ταυτόχρονα το υπάρχον καθεστώς ενεργειακού συμψηφισμού (net-metering) θα αντικατασταθεί από μία όχι ιδιαίτερα συμφέρουσα επιχορήγηση, είναι απαραίτητο για τους πολίτες να αναζητήσουν νέες ευκαιρίες στον τομέα των φωτοβολταϊκών συστημάτων. Αν και ο αριθμός των φωτοβολταϊκών εγκαταστάσεων αυξάνεται καθημερινά, ξεπερνώντας τα 4MW εγκατεστημένης ισχύος το 2018, ένας μεγάλος αριθμός Ολλανδών βρίσκονται μακριά από αυτές τις εξελίξεις.

Η παρούσα διπλωματική εργασία περιλαμβάνει την μοντελοποίηση της έκθεσης επιχειρησιακής σκοπιμότητας φωτοβολταϊκών εγκαταστάσεων, με στόχο να παρέχει στους πολίτες έναν εύκολο, δωρεάν και άμεσο τρόπο να εκτιμήσουν τις προοπτικές κτηρίων στον τομέα αυτό. Σε πρώτη φάση, χρησιμοποιώντας τον αλγόριθμο MASK R-CNN, απομονώνονται και εξάγονται οι διαθέσιμες οροφές από δορυφορικές εικόνες, με επιτυχία 77.94% κατά μέσο όρο. Στη συνέχεια, μέσω της χρήσης της βιβλιοθήκης PnLib της Python, επιλέγονται τα κατάλληλα στοιχεία για την εγκατάσταση και προσομοιώνεται η απόδοση του συστήματος κατά τη διάρκεια των επόμενων δέκα ετών για ένα οικιστικό συγκρότημα στο Hoofddorp, στα νότια του Άμστερνταμ. Ο στόχος αυτής της διπλωματικής είναι η δημιουργία ενός γενικού πλαισίου για την προσομοίωση της απόδοσης φωτοβολταϊκών συστημάτων που θα ενσωματωθεί στο μέλλον σε μια διαδικτυακή εφαρμογή-εργαλείο για την διευκόλυνση τέτοιου τύπου εγκαταστάσεων.

“We just can't seem to stop burning up all those buried trees from way back in the carboniferous age, in the form of coal, and the remains of ancient plankton, in the form of oil and gas. If we could, we'd be home free climate wise. Instead, we're dumping carbon dioxide into the atmosphere at a rate the Earth hasn't seen since the great climate catastrophes of the past, the ones that led to mass extinctions. We just can't seem to break our addiction to the kinds of fuel that will bring back a climate last seen by the dinosaurs, a climate that will drown our coastal cities and wreak havoc on the environment and our ability to feed ourselves. All the while, the glorious sun pours immaculate free energy down upon us, more than we will ever need. Why can't we summon the ingenuity and courage of the generations that came before us? The dinosaurs never saw that asteroid coming. What's our excuse?”

- Neil DeGrasse Tyson

TABLE OF CONTENTS

ACKNOWLEDGEMENTS	v
ABSTRACT	vii
ΠΕΡΙΛΗΨΗ	viii
LIST OF FIGURES	xiii
LIST OF GRAPHS	xiv
LIST OF TABLES	xv
LIST OF EQUATIONS	xvi
1. INTRODUCTION	1
1.1 Background Information	1
1.2 Statement of Challenges	3
1.3 Literature Review	3
1.3.1 Google's Project Sunroof	4
1.2.1 Rooftop Detection SVM	4
1.2.3 Dutch PV Portal 2.0	5
1.4 Thesis Outline	5
2. THE CASE OF THE NETHERLANDS	7
2.1 The electricity market in the Netherlands until 2004	7
2.2 The liberalized Dutch power sector: 2004 - Today	8
2.3 Legal and policy context	9
3. COMPUTER VISION	13
3.1 Convolutional Neural Networks	13
3.1.1 Tensor Vectorization	13
3.1.2 The architecture	14
3.1.3 Gradient Descent	15
3.1.4 Stochastic Gradient Descent	16
3.1.5 Error back propagation	17
3.1.6 The ReLU Layer	18
3.1.7 The Convolution Layer	20
3.1.8 Why convolute?	21
3.1.9 Fully connected layer	22
3.2 From Sliding Windows to Mask R-CNN	22
	x

3.2.1 Sliding-window detectors	22
3.2.3 Pooling layer	23
3.2.4 Fast R-CNN	25
3.2.5 RoI Pooling	25
3.2.6 Faster R-CNN	26
3.2.7 Region Proposal Networks	26
3.2.8 Mask R-CNN	29
4. ANNUAL ENERGY YIELD CALCULATION	31
4.2 The effect of physical phenomena	32
4.2.1 Air Mass	32
4.2.2 Solar Position	32
4.2.3 Solar radiation	33
4.2.4 Temperature	34
5. METHODOLOGY	36
5.1 Overview	36
5.2 Image loading	36
5.3 Model Implementation	38
5.3.1 Detection	39
5.3.2 Visualization	41
5.4 Model Training and Evaluation	42
5.4.1 Training using two distinct datasets	42
5.4.2 Evaluation Process	43
5.5 Photovoltaic system modeling	44
5.5.1 Pvlib python	44
5.5.2 Modeling Air Mass and Solar Position	44
5.5.3 Solar Radiation Models	45
5.5.4 Temperature Model	47
5.6: PV Module and Inverter selection	48
5.6.1: PV Module Selection	48
5.6.2: Inverter Selection	49
6. RESULTS	51
6.1 Mask R-CNN Accuracy	51
6.2 Energy Yield	54

7. CASE STUDY: RESIDENTIAL BUILDING IN HOOFDDORP	56
8. CONCLUSIONS AND FUTURE PROSPECTS	62
REFERENCES	63
APPENDIX	69

LIST OF FIGURES

Figure 1: Solar energy potential throughout the Netherlands [6]	2
Figure 2: Illustration of the convolution process [17]	21
Figure 3: System flow for the sliding-window detector [22]	23
Figure 4: Max pooling with a 2×2 pooling window [24]	24
Figure 5: Workflow of fast R-CNN [22]	25
Figure 6: Faster R-CNN architecture [22]	26
Figure 7a: Faster R-CNN workflow with RPN usage highlighted.	29
Figure 7b: Region proposal network workflow [27]	29
Figure 8: Mask R-CNN architecture [20]	30
Figure 9: Energy production losses [29]	31
Figure 10: A stepwise approach in annual energy yield calculation	32
Figure 11: Flow chart of the detection process	40
Figures 12a-12f: Demonstration of the detection and visualization process	41
Figures 13a-13b: Demonstration of two distinct cases of misclassification	51
Figure 14: Model performance under the second dataset	52
Figure 15: Demonstration of the model's performance in the identification of a large storehouse	53
Figures 16a, 16b: A case of misclassification	54
Figures 17a, 17b: Residential building in Hoofddorp	56
Figure 18: Estimated rooftop area using "Google Maps Area Calculator Tool"	57

LIST OF GRAPHS

Graph 1: Market share of electricity Distribution System Operators (DSOs) in the Netherlands in 2016 [15]	8
Graph 2a, 2b: Allocation of energy consumption thanks to net-metering [16]	10
Graph 3: Electricity prices for households in the Netherlands from 2010 to 2018, semi-annually [15]	11
Graph 4: Illustration of the gradient descent method [17]	17
Graph 5: The ReLU function [17]	19
Graph 6: Azimuth, zenith angles, solar elevation and equation of time for the Amsterdam Area in 2018	45
Graph 7: Comparison of the clear sky models available in pvlib	46
Graph 8: GHI, DNI and DHI values for the 2018 annual year using Ineichen and Perez clear sky model	46
Graph 9: PV power output related to temperature	47
Graph 10a: System energy production for an average year	60
Graph 10b: Real-time system efficiency losses	60

LIST OF TABLES

Table 1: SDE+ scheme	11
Table 2: Information regarding zoom level	37
Table 3: Average monthly temperatures in the region of Amsterdam [31	46
Table 4: Accuracy results in four different scenarios	53
Table 5: Type of household appliances and respected capacities	58
Table 6: PV installation case study	60

LIST OF EQUATIONS

Equation 1: Abstract description of CNN's structure	14
Equation 2: Prediction output	15
Equation 3: GD output	15
Equation 4: Truncation function	18
Equation 5: indicator function	18
Equation 6: ReLu function	18
Equation 7: Logistic sigmoid function	19
Equations 8a, 8b: Max and average pooling	24
Equation 9: RCN loss function	28
Equation 10: $smooth_{L_1}(x)$	28
Equation 11: Annual energy yield estimation	31
Equation 12: Zenith angle calculation during solar noon	33
Equation 13: Alternative zenith angle formula	33
Equation 14: Extraterrestrial radiation	33
Equation 15: Global Horizontal Irradiance	34
Equation 16: Meters per pixel ratio	37
Equation 17: Rooftop's acreage	37
Equation 18: Margin of error	44
Equation 19: Prediction accuracy	44
Equation 20: Kasten and Young air mass model	44
Equation 21: Ineichen and Perez model	45
Equation 22: Power of inverter	50
Equation 23: ROI calculation	61

ACRONYMS

AC:	Alternative Current
ACM:	Authority for Consumers and Markets
AM:	Air Mass
API:	Application Programming Interface
BOS:	Balance of Systems
C:	Celsius
CNN:	Convolutional Neural Network
DC:	Direct Current
DHI:	Diffuse Horizontal Irradiance
DNI:	Direct Solar Irradiance
DOY:	Day Of the Year
DSO:	Distribution System Operator
EDC:	Energy Distribution Company
fc:	fully-connected
FAIR:	Facebook AI Research
FCN:	Fully Convolutional Network
FPN:	Feature Pyramid Network
GD:	Gradient Descent
GHI:	Global Horizontal Irradiance
GW:	GigaWatts
IoU:	Intersect over Union
kV:	kiloVolts
KW:	KiloWatts
KWh:	KiloWatt hours
MW:	MegaWatts
ms:	milliseconds
NEM:	Net Energy Metering
NREL:	National Renewable Energy Laboratories
ODE:	Opslag Duurzame Energie

PS:	Project Sunroof
ReLU:	Rectified Linear Unit
ROI:	Return Of Investment
RoI:	Region of Interest
R-CNN:	Region-based Convolutional Neural Network
RPN:	Region Proposal Network
SGD:	Stochastic Gradient Descent
SPA:	Solar Position Algorithm
SS:	Selective Search
SVM:	Support Vector Machine
USD:	United States Dollar
W:	Watts

1. INTRODUCTION

1.1 Background Information

In the recent years, the imminent depletion of fossil fuels paired with the repercussions of an oil-based economy are leading causes of concerns for the whole world. On many countries, especially in the west, transportation, heating, and electricity generation are tightly tied to the oil reserves, which are fixed since petroleum is naturally formed far too slowly to be replaced at the rate at which it is being extracted [1]. Furthermore, the detrimental environmental effects of oil, due to its toxicity, contribute to phenomena like air and sea pollution, acid rain and greenhouse effect, while benzene exposure is closely linked to birth defects, terminal leukemia, Hodgkin's lymphoma, and other blood and immune system diseases [2]. These reasons, and many more, fuel the transition of the world towards 100% renewable energy sources and a sustainable, circular economy. According to Grin et al., a sustainability transition is defined as a “radical transformation towards a sustainable society, as a response to a number of persistent problems confronting contemporary modern societies” [3].

During these events, the Netherlands, a country known for its windmills and green energy faces its own struggles: despite common beliefs, only 7% its energy consumption comes from renewable sources, indicating that the 2020 goals on renewable energy production and greenhouse gas emissions won't be met. This realization coincides with the replacement of the current net-metering scheme (SDE+) with a return subsidy, which will gradually fade during the next ten years. Furthermore, even though the number of solar energy installations increases day to day, with the installed capacity overpassing 4 MW, a great number of Dutch people has not ventured towards that direction yet [4].

But why solar? Solar energy is radiant light and heat from the Sun that is harnessed using a range of ever-evolving technologies such as solar heating, photovoltaics, solar thermal energy, solar architecture, molten salt power plants and artificial photosynthesis. It is an important source of renewable energy and its technologies are broadly characterized as either passive solar or active solar depending on how they capture and distribute solar energy or

convert it into solar power. Active solar techniques include the use of photovoltaic systems, concentrated solar power and solar water heating to harness the energy. Passive solar techniques include orienting a building to the Sun, selecting materials with favorable thermal mass or light-dispersing properties, and designing spaces that naturally circulate air [5].

In the Netherlands, wind energy has seen a massive rise during the past few years, but solar energy stays somewhat behind. Even though, naturally, we consider the Netherlands a sun-less country, the data presented by SolarGIS in the next picture (Figure 1) show a different case. Even though irradiation levels do not reach those of Mediterranean countries, there is a lot of potential for solar installations, particularly in the middle-southern part of the country.

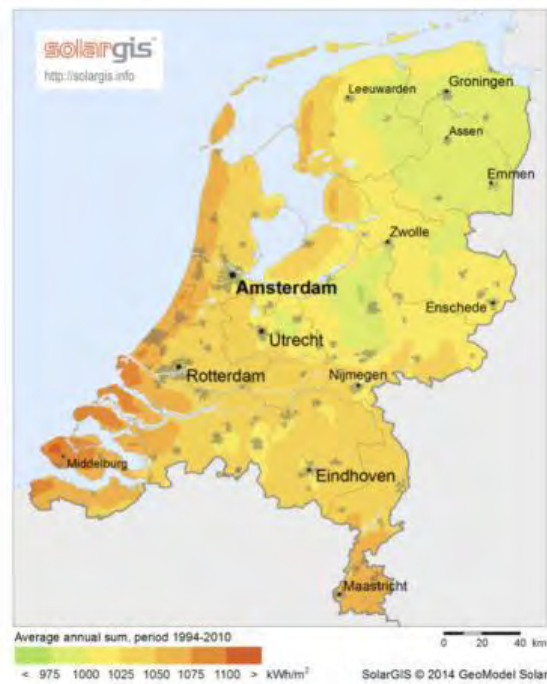


Figure 1: *Solar energy potential throughout the Netherlands [6]*

Moreover, solar energy has some clear advantages over wind farms. Powering ones neighborhood or home with wind turbines is not a simple process, since turbines require planning and building approval and, due to their height and noise, are often not allowed to be installed in or near residential areas. In addition, good sites for wind turbines are hard to find, because of their need to be clear from ground obstructions that affect the wind. On the contrary, a photovoltaic installation, especially a grid-connected one, is a much simpler

process, since solar panels are allowed to be installed on most rooftops and the investment and recurring maintenance costs are significantly lower.

1.2 Statement of Challenges

In our mission to help this process along the way, we decided to create a solar business case analyzer: by using computer vision techniques and Mask R-CNN, we are able to extract rooftops from satellite imagery and, as a next step, simulate the performance of a solar energy system installation in the selected area. The scope of this thesis is to provide a free, accurate and easy-to-use tool to people who hesitate to take the first step towards solar energy. The analyzer can be proven particularly useful in the case of people who desire to remove the “middle man” from the process of the photovoltaic system installation, providing them with the optimum choice of installation components, settings and configurations, as well as a break-down of all costs and earnings during a 10-year period. It is especially interesting to research the economic viability and feasibility of such a project, given that in the Netherlands the existing net-metering scheme will no longer be the case from 2020 and onwards. Instead of giving the small-scale renewable energy producers the possibility to offset 100% of the generated energy from their total energy bill, the netting limit will drop to 70% in 2020 and will be gradually reduced to 0%. The remaining generated energy will be sold to the Distribution System Operators (DSOs) for predefined feed-in tariffs, which will also reduce with time. More information regarding the present situation and future regulations can be found in chapter 2.

1.3 Literature Review

Commercial applications utilizing computer vision only started to appear within the last decade. This is hardly a surprise, since computer vision itself is a new scientific field, with its origins traced back only 50 years ago [8]. Consequently, the number of computer vision rooftop detectors that combine detection with PV yield simulation is quite limited. Among

them, Google's Project Sunroof is the one which stands out, but European countries are not yet available as an option. Moreover, a rooftop recognition implementation using SVM machine learning algorithm, a quite popular algorithm for image segmentation tasks before the rise of computer vision. Finally, one option which focuses specifically on the Netherlands is a tool developed by TU Delft, the Dutch PV Portal 2.0, which provides real-time weather data and PV system design simulations.

1.3.1 Google's Project Sunroof

In 2015, Google INC launched Project Sunroof (PS), a web-based application aiming to provide consumers with an estimation of annual savings in terms of electricity bills, when solar panels are installed on their rooftop and can be considered the only computer vision based application commercially available which serves this purpose. In order to achieve that, PS uses imagery from Google Maps and Google Earth and through computer vision, 3D modeling and machine learning create a solar score for every rooftop that it maps. This score is calculated taking into account the amount of sunlight received by each portion of the sunroof during the course of a year, local weather patterns, sun's position in various day-times and, eventually, shading from the surrounding environment like trees, buildings etc. [8]. Finally, the estimated score is translated into potential energy production. A recommendation regarding installation size is given based on local electricity and personal billing rates plus the rooftops potential while the installation costs and payback period are calculated. Additionally, Google's' application provides direct comparisons between finance options and direct links to providers. At the time of writing, PS is available only in the US and covering 50 states [8]. However, Google plans to expand PS to a global scale during the next years.

1.2.1 Rooftop Detection SVM

In 2013 Hayk Baluyan, Bikash Joshi, Amer Al Hinai, and Wei Lee Woon released a paper demonstrating rooftop segmentation from satellite images using an SVM approach. Regions of Interest (ROIs) were generated using k-Means clustering in order to divide the pixels of the input image into k clusters based on color and later adopting the flood-fill algorithm

organize the pixels within a cluster into a set of regions. After a feature extraction process, an SVM classifier is applied to distinguish rooftop from non-rooftop regions. Lastly, a histogram method is used for detection rooftops that the SVM kernel may have declassified. The accuracy score of this approach measured to be 76% [9]. The model seems to struggle when a rather large rooftop relative to the input image size appears and in cases of rooftops with a color variation.

1.2.3 Dutch PV Portal 2.0

TU Delft's Dutch PV Portal 2.0 was created by the Photovoltaic Materials and Devices group of Delft University of Technology. The goal of this research was to provide publically accessible information on solar energy in the Netherlands, combining the expertise of the PVMD group with real-time and historical data provided by the Royal Netherlands Meteorological Institute. The simulations performed by the portal do not include specific components of the system, but take into account the panel technology, location, surface area, tilt and azimuth to create a realistic assessment of the potential solar energy yield.

1.4 Thesis Outline

In Chapter 1, there is an introduction to the overall approach of the research topic, highlighting the current situation and the reasoning behind the selection of this topic. Also, in different subsections, we include a literature review, examining similar projects in the field and clearly define the challenges of the project.

Chapter 2 includes the presentation of the situation in the Netherlands now, an analysis of the imminent changes in the existing netting scheme and how these will affect renewable energy generation in the future.

In Chapter 3, an in-depth description of utilized computer vision methods and techniques is discussed, covering the transition of our research through different algorithms to Mask R-CNN.

Chapter 4 encompasses the processes we used to calculate the energy yield of each potential PV system installation, including the different losses that are included in the model and other factors that affect its efficiency.

In Chapter 5, we describe the methodology used to implement and assess each specific case, starting from the rooftop extraction from satellite images and concluding with the implementation of 10-year scenario regarding the energy output of the system.

Moving on to Chapter 6, an extensive presentation and assessment of our final results takes place, including the benchmarking of our models and used algorithms in order to examine their efficiency.

In order to test our assumptions and results, in Chapter 7 we opted to research the case study of a residential, medium-sized, south-oriented building in Hoofddorp, near Amsterdam, define the optimum components, settings and configurations in the building and assess the return of investment of the installation during the next ten years.

Finally, conclusions and recommendations for future work are included in Chapter 8.

2. THE CASE OF THE NETHERLANDS

2.1 The electricity market in the Netherlands until 2004

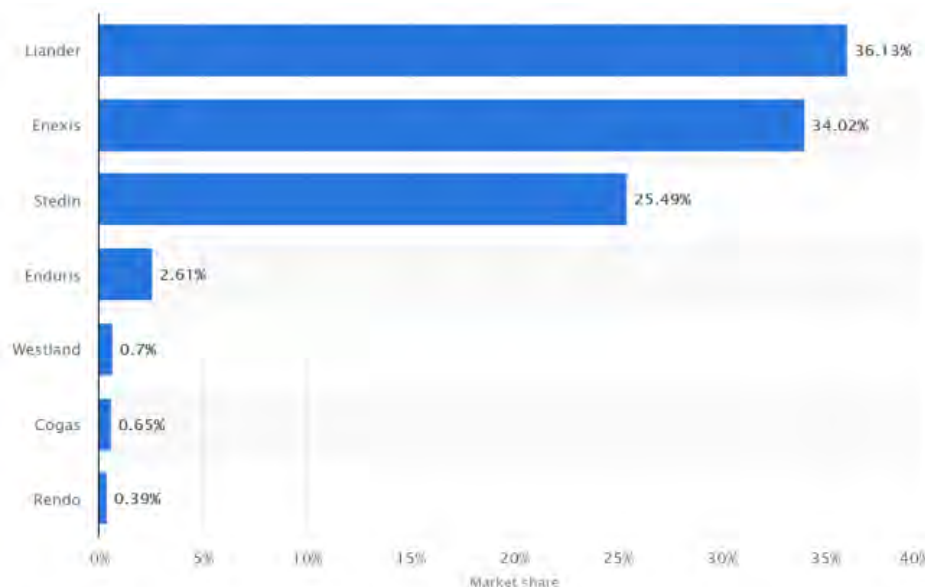
Nowadays, the Dutch energy market offers an abundance of choices and opportunities for small and large scale electricity consumers. The power sector is comprised of more than 45 energy suppliers, that each offer different rates and contract conditions [11]. However, up until recent years, the situation in electricity production and distribution was drastically different. Until the beginning of the 20th century, the Dutch customers did not have the possibility of selecting their preferred energy supplier. Instead, responsible for the supply and balancing in each different province of the country was a specific utility assigned by the government [12]. Additionally, before 1998, utilities were allowed to own an electricity network, transmit, distribute and sell the electricity concurrently. According to Foxon, under this national system, a large-scale optimization was not feasible, since *“every regional unit was responsible for balancing supply and demand in its own region”* [13]. This, essentially, meant that companies who owned part of the network were easily able to commercially dominate those who were only active in the retail field. As a result, four companies, Essent, Eneco, Nuon and Delta eliminated the competition and monopolized the energy market in regions where each one owned the network.

The liberalization of the Dutch power sector took place in July 2004 and was heavily fueled by the Electricity Act of 1998, which demanded the separation between the network ownership and the electricity supply and provided consumers with the opportunity to select their preferred electricity supplier [14, pp. 94]. Tõnurist et. al. confirm that the change would happen gradually, as a large part of the consumers would have the right to make their own decision by 2002, followed by some commercial users in 2004 and finally, households, in 2018 [14]. Furthermore, they affirm that even though at first the reform was supposed to be applied to green-energy providers only, conventional electricity producers followed shortly. This period marked the start of the detachment of the distribution and transmission of generated energy from the fields of metering, trade and sales, following the EU electricity directive (2003/54/EC) [14, pp. 94-95]. The new state provided an incentive for companies to be competitive, offer better customer support and regulate electricity prices.

2.2 The liberalized Dutch power sector: 2004 - Today

Following the years from 2004 and onwards, the electricity production and retail in the Netherlands were liberalized. Nevertheless, the fields of energy transmission and distribution remain centralized and operated by the Transmission System Operator (TSO) and the Distribution System Operators (DSOs) respectively.

Nowadays, *TenneT B.V.*, owned solely by the Dutch government, is the only stakeholder responsible for operating the 380 kV and 220 kV high-voltage grid throughout the Netherlands and its interconnections with neighboring countries, as well as the 150 kV grid in the province of South Holland. The sole shareholder of the company is the Dutch Ministry of Finance which is also responsible for its subsidiary, *TenneT TSO GmbH*, one of Germany's four transmission system operators. As far as DSOs are concerned, at the moment there are seven Dutch utility companies which own the regional energy grids: *Cogas Infra en Beheer B.V.*, *Enduris B.V.*, *Enexis B.V.*, *Liander N.V.*, *Stedin B.V.* and *Westland Infra Netbeheer B.V.* Judging from the following barplot (Graph 1), it is apparent that three dominant DSOs manage more than 95% of customers' connections, with Liander leading the way, followed shortly by Enexis [15].



Graph 1: Market share of electricity Distribution System Operators (DSOs) in the Netherlands in 2016 [15]

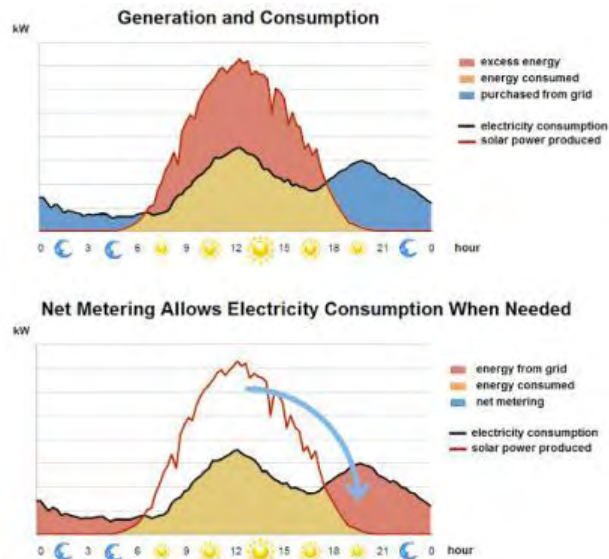
The system operator and the utility companies still hold a monopoly position in the energy market. Customers can opt for the electricity retailer that better fits their needs, but the DSOs are still assigned regionally. As a result, to guarantee the rights of consumers and businesses in the energy sector and their ethical behaviour in this field, these parties have to be regulated. This necessity led to the creation of the Authority for Consumers and Markets, in 2013.

2.3 Legal and policy context

The Dutch photovoltaic energy market experiences the greatest growth of its history, with 1.3-1.5 GW expected increase in installed power in 2018. For the first time ever, the installed PV power is presumed to have surpassed 4 GW, which marks the entry of the Netherlands into Europe's gigawatt club alongside Germany, Italy and others. This great milestone is largely driven by the Stimulerings Duurzame Energieproductie, also known as SDE+ subsidy, which allows for net-metering (NEM). *Salderingsregeling* or net-metering basically means that the energy supplier will only consider the balance of purchased and returned energy when charging the consumption costs. It is a way for consumers who produce part or all of their own electricity to consume generated power anytime, instead of only the moment it is produced. This policy proves to be particularly beneficial and motivating, principally in the cases of solar and wind installations, which are non-dispatchable (when not directly connected to storage options, like considerably sized batteries). Net-metering credit can be either monthly or annual, allowing consumers to use power generated in sunnier periods of the year anytime it is needed, just like an exchange.

This arrangement is particularly advantageous for customers, since not only they accumulate considerable savings, but also avoid energy transportation costs and do not get charged with any kind of taxes (energy tax, storage of renewable, etc.). Graphs 2a and 2b demonstrate the allocation of energy generation and consumption due to net-metering. The SDE+ scheme was introduced in 2004 and will be concluded at 2020. The Dutch government intends to replace the current netting scheme with the Stimuleringsregeling Duurzame Energietransitie (SDE++) reform, which is essentially a return subsidy for technologies that compete on a reduction of CO₂ emissions basis and not on generated renewable energy amount. Applications will be open throughout the year and the subsidy ceiling will be predetermined

annually. Furthermore, a cap on how much surplus power may be injected into the grid will be enforced, since the current network cannot store and support the ever-increasing amounts of power [6].



Graph 2a, 2b: Allocation of energy consumption thanks to net-metering [16]

For the time being, the subsidy is applicable to all small case producers of biomass, geothermal, water, wind and solar energy who fulfill the following criteria:

- Having a connection of up to and including a maximum of 3 x 80 A.
- Having a single, bi-directional meter that can measure the current flowing in two directions installed and in functioning order. A smart meter is currently not compulsory, though that is going to change from 2021 and onwards.

Initially, there was a netting limit of 3000 kWh per connection, which was shifted to 5000 kWh (Samson amendment) and then was altogether negated as of July 1st, 2013. The maximum netted amount of generated electricity now equals the consumer's own consumption. If more energy is generated than one's own consumption, the electricity supplier is responsible for buying the excess energy for a reasonable fee, which is called *feed-in tariff*. It is important to point out that, at the moment, the feed-in tariff is determined separately by each dutch utility. On Graph 3 below we can see the prices for electricity up

until this year, where a decreasing trend is quite apparent, except for 2018, where the price per kWh increased quite a bit.



Graph 3: Electricity prices for households in the Netherlands from 2010 to 2018, semi-annually [15]

The way that the SDE++ scheme is going to work in the future is better depicted in Table 1 below (which is unfortunately only available in Dutch).

SDE++ scheme:

Jaar	2020	2021	2022	2023	2024	2025	2026	2027	2028	2029	2030
Variant B (% saldering)	70%	60%	60%	55%	50%	40%	35%	25%	20%	15%	12% ¹
Variant C (teruglever-subsidie in €ct/kWh)	0,12	0,11	0,1	0,1	0,09	0,08	0,07	0,05	0,04	0,03	0,02 ²

Table 1: SDE+ scheme [15]

Basically, the scheme will work by imposing an annual netting limit on the total of produced energy. Starting from 2020, the netting limit will decrease every year, starting at 70%. This means that on 2020 the customers will be allowed to net 70% of their produced energy,

essentially selling it for the same price that they buy it. The remaining 30% will be bought from the DSOs for a predefined feed-in tariff, which in the case of 2020 will be 0.12 ct/kWh. It is quite apparent that the aim of this measure is to discourage the customers from feeding in the grid. This is due to the fact that, in the long term, the most sustainable solution for energy distribution is the maximization of self-consumption. On chapter 4, will conduct a case study to examine the viability of solar energy system in the future without the inclusion of a battery system for the time being.

3. COMPUTER VISION

During the past decade, computer vision has revolutionized image detection applications. In this section, the theory behind computer vision algorithms is discussed starting from the task of image classification and convolutional neural network (CNN) architectures, a necessary step for understanding computer vision, and in the process unravelling the steps that led to Mask R-CNN algorithm.

3.1 Convolutional Neural Networks

Even though CNNs are being used widely in various applications, the most common purpose of such algorithms is related with imagery tasks, with the most notable being image classification, image semantic segmentation, and object detection among others. For now on though, the main focus would be image classification (or categorization). In this task, every image has a major object which occupies a large portion of itself. Hence, it is safe to assume that the image can be classified based on the identity of its main object, e.g., car, dog, cat, train, etc. [17, Ch. 1, pp. 5].

3.1.1 Tensor Vectorization

According to DoitPoms platform, a teaching initiative by the Cambridge University, tensors are simply mathematical objects that can be used to describe physical properties, just like scalars and vectors. In fact, tensors can be considered a generalization of scalars and vectors; a scalar is a zero-rank tensor, and a vector is a first rank tensor [18].

A tensor's order (rank) is determined by the number of directions (and therefore the dimensionality of the array) needed to explain it. For instance, an order 1 tensor is a property that can be fully expressed by an $n \times 1$ column vector (one direction), an order 2 tensor is a property that can be fully expressed by $n \times n$ tensor (two directions), etc. [18].

Images can be essentially considered as order 3 tensors due to their RGB format. A third order tensor contains HWD elements, and every one of them can be classified by an indication triplet (i, j, d) , with $0 \leq i < H, 0 \leq j < W, 0 < d < D$. A way to view a tensor of that order is to treat it as it is containing D channels of matrices according to Jianxin Wu et. al [17, Ch. 2.1, pp. 2]. Each individual channel is a matrix with a size $H \times W$, with the first channel having the numbers of the tensor that are classified by $(i, j, 0)$. Note that when $D = 1$ the tensor decreases to a matrix [17, Ch. 2.1]. Thus, a color image with H rows and W columns is a tensor with size $H \times W \times 3$. If the image is stored in the RGB format, 3 channels can be distinguished (for R, G, B, individually), while each channel being an $H \times W$ matrix (second-order tensor) that holds the R (or G, or B) values of all pixels (first order tensor) [17, Ch. 2.1, pp. 3].

It is always helpful to represent an image as a tensor. In the early years of computer vision, images were often converted to their gray-scale counterpart (which is a matrix instead of a third order tensor) since it was easier to process. Nevertheless, color information is crucial in any image or video recognition tasks. Various computer vision architectures need to process color in a principled way [17, Ch. 2.1, pp. 4].

3.1.2 The architecture

Ordinarily, a CNN receives as an input a third-order tensor of H rows, W columns and 3 channels (Red, Green, Blue color channels). The input then sequentially goes through a set of processing

steps called layers. An abstract composition of CNN's structure is given below:

$$\mathbf{x}^1 \longrightarrow \boxed{\mathbf{w}^1} \longrightarrow \mathbf{x}^2 \longrightarrow \dots \longrightarrow \mathbf{x}^{L-1} \longrightarrow \boxed{\mathbf{w}^{L-1}} \longrightarrow \mathbf{x}^L \longrightarrow \boxed{\mathbf{w}^L} \longrightarrow z$$

Equation 1: *Abstract description of CNN's structure.*

The above equation highlights how a CNN runs layer by layer in a forward path. \mathbf{x}^1 is the input (in this case an image) and goes through the processing in the white box which is the first layer. All the parameters associated with the first layer's processing are denoted as \mathbf{w}^1

tensors. x^2 is the output of the first layer, which also serves as an input for the second layer. The process continues until the final product, x^L is reached. Still, a final layer is added for a method called back propagation, which learns good parameter values [17, Ch. 3.1, pp. 3]. The last layer can be considered as loss layer. If the corresponding target (ground-truth) value is t for the original input x^1 , then a loss function can be used in order to estimate discrepancy between the prediction x^L made by the CNN and the target t [17, Ch. 3.1, pp. 4]. When all parameters w^1, \dots, w^{L-1} of a CNN model have been “learned”, the model is ready to make predictions. Predictions are made by running through the CNN in a forward notion. When x^L is calculated, which contains the probabilities of x^1 belonging to one of the target categories, the predictions can be outputted as:

$$\text{argmax}(x_i^L)$$

Equation 2: *Predictions output.*

Last but not least, the loss layer is only necessary for the learning process and does not participate in the prediction estimation [17, Ch. 3.2].

3.1.3 Gradient Descent

As mentioned above, the parameters of a CNN are optimized to minimize the loss function. When we go through a CNN for the first time, the prediction is made using only the initial CNN’s parameters. After that the prediction is compared with the target t corresponding to x^1 and the loss z is calculated. The loss z is then a supervision signal, guiding how the parameters of the model should be modified (updated) using gradient descent (GD) function [17, Ch. 3.3, pp. 2]. The GD function’s equation is given below:

$$3w^i \leftarrow w^i - n \frac{\partial z}{\partial w^i}$$

Equation 3: *GD output.*

The partial derivative $\frac{\partial z}{\partial w^i}$ or gradient calculates the rate of increase of z with respect to the changes in different dimensions of w^i [17, Ch. 3.3, pp. 5]. Given a small local area throughout the current value of w^i , moving w^i towards the direction that the gradient indicates, will result in increasing the value of the loss function. Hence, in order to achieve minimization, w^i should be updated in the opposite direction that the gradient indicates. This updating process is called gradient descent. A visual demonstration of this method can be found in graph 5, where the gradient is denoted by g . However, if the step being taken surpasses a certain threshold, namely leading too far in the negative gradient direction, z may increase. Consequently, the parameters should be changed only by a small portion of the negative gradient, controlled by the learning rate $\eta > 0$ which is normally initialized by a small value (0.001) [17, Ch. 3.3, pp. 6]. When all training samples have been used to update the internal model parameters, an epoch has been processed. According to Jason Brownlee, the number of epochs is a hyperparameter that defines the number of times that the learning algorithm will work through the entire training dataset [19]. An epoch will usually contribute in the average z 's reduction. Thus, the number of epochs is normally great (100 - 1000), deducting the learning algorithm to run until the model's error has been adequately minimized [19].

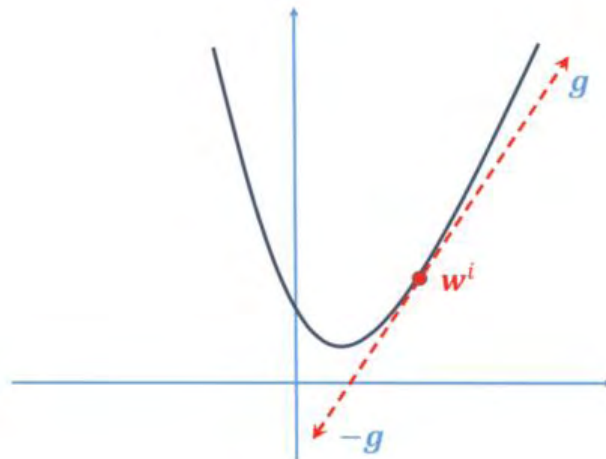
3.1.4 Stochastic Gradient Descent

Even though gradient descent may be simple in terms of mathematical complication, in practice it can be a challenging process. For instance, if only one training sample is used for the gradient calculation and parameters updating, an unstable loss function will occur. In order to avoid this, small subsets of the main training set can be used in estimating the gradient and before applying it to update the parameters. This method is called Stochastic Gradient Descent (SGD). However, SGD requires many computations in this batch approach since the parameters are updated only every epoch, making it impractical particularly for quite large datasets [17, Ch. 3.3, pp. 7]. A settlement is to use small batches of training samples called mini-batches. Mini-batch SGD is considered the most common method in CNN's parameters updating. Note that in this case, the input tensor's order is increased by one ($H \times W \times 3 \times S$, where S is the mini-batch size) [17, Ch. 3.3, pp. 8].

3.1.5 Error back propagation

The partial derivative corresponding to the last layer ($\frac{\partial z}{\partial w^L}$) can be calculated with ease, considering x^L is related to z directly under the control of parameter w^L , something that is also applicable with $\frac{\partial z}{\partial w^L}$ [17, Ch. 3.4, pp. 1]. In fact, these two partial derivatives are calculated for every layer.

- The term $\frac{\partial z}{\partial w^i}$ is used for updating the parameters corresponding to the current layer (i -th).
- The term $\frac{\partial z}{\partial x^i}$ is used for updating the parameters backwards, for instance, the $(i - 1)$ -th layer. A more intuitive approach is: x^i is the output of the $(i - 1)$ -th layer and $\frac{\partial z}{\partial w^i}$ is how x^i should be changed in order to reduce the loss function. Thus, $\frac{\partial z}{\partial x^i}$ can be viewed as the part of the “error” supervision information propagated from z to backward, until the current layer is reached, in a chained layer by layer manner [17, Ch. 3.4, pp. 2].



Graph 4: Illustration of the gradient descent method [17]

3.1.6 The ReLU Layer

The ReLU is not a separate segment of CNN's process. In fact, it is an additional level in the convolutional procedure. The main purpose of this layer is to increase the non-linearity in an image. Images are simply not linear. The transition within pixels and colors are obvious examples of linearity. Thus, the ReLU function assists in breaking up that linearity [20]. If this layer is noted as the l -th layer, the ReLU is a function that transforms the input x^l to output y with both of these properties, sharing the same size. Then, a truncation applied independently for every element in the input is made:

$$y_{i,j,d} = \max(0, x_{i,j,d}^l)$$

Equation 4: *Truncation function.*

with $0 \leq i \leq H^l = H^{l+1}$, $0 \leq j \leq W^l = W^{l+1}$, and $0 \leq d \leq D^l = D^{l+1}$ [17, Ch. 5, pp. 1]. Note that since there is not any parameter inside a ReLU layer, there is not any need for parameter learning.

Based on the previous equation:
$$\frac{dy_{i,j,d}}{dx_{i,j,d}^l} = [x_{i,j,d}^l > 0]$$

Equation 5: *indicator function.*

Inside the brackets is the indicator function which is 1 when its argument is true and 0 otherwise.

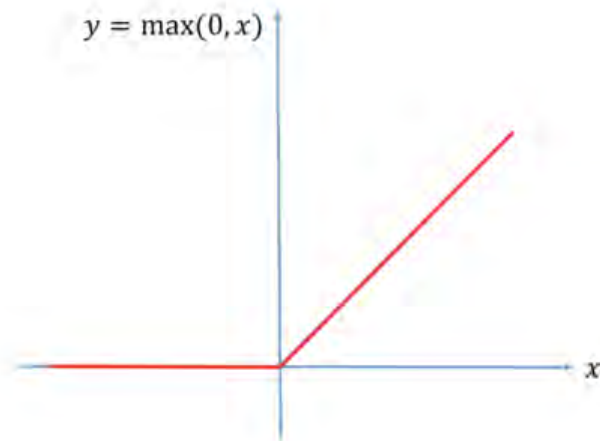
Therefore:

$$\left[\frac{\partial z}{\partial \mathbf{x}^l} \right]_{i,j,d} = \begin{cases} \left[\frac{\partial z}{\partial \mathbf{y}} \right]_{i,j,d} & \text{if } \mathbf{x}_{i,j,d}^l > 0 \\ 0 & \text{otherwise} \end{cases} .$$

Equation 6: *ReLU function.*

Note that y is equivalent to x^{l+1} [17, Ch. 5, pp. 3]. Relu function is visually demonstrated in Graph 6.

In practice, the above equation implies that $y_{i,j,d}^l$ will be activated only if an image has certain patterns ,for instance a cat's ears or an airplane's wings, that match. This process is achieved by, letting $x_{i,j,d}^l$ be positive if a section within the input image is identified to have these kinds of patterns and negative or zero otherwise. The ReLU layer will set all negative values to zero. As a result, this processing step provides an early hint on whether the input image contains the target object or not [17, Ch. 5].



Graph 5: The ReLU function [17].

There are numerous additional nonlinear transformation methods being used widely in neural networks architectures. A common example can be regarded as the logistic sigmoid:

$$y = \sigma(x) = \frac{1}{1 + \exp(-x)}$$

Equation 7: Logistic sigmoid function.

However, research suggests that logistic sigmoid works significantly inadequate in CNNs. A sigmoid layer will produce in a vital reduction to the magnitude of the gradient, which will end up 0 in many layers, making gradient-based learning (SGD) very tough. In contrast,

the ReLU only sets the gradient of insignificant features in the l -th layer to 0, allowing back propagation only for the activated ones, while keeping them unchanged. The replacement of sigmoid with ReLU was a great development in CNN's design not only providing a decreased difficulty in learning the parameters but also boosting the predictive ability of the model [17, Ch. 5].

3.1.7 The Convolution Layer

The Convolution layer is the main building piece of a CNN and it is responsible for most of the computational heavy lifting. It contains an assortment of learnable filters called feature detectors which are order 3 tensors with a size of $H \times W \times 3$. Through the forward run of the input, its filter is slid across the surface of the input and the dot products between the indexes of the filter and the input are computed for all the available positions. This method will produce a 2-dimensional feature map that holds the responses of the filter at every spatial position. The aforementioned sliding process is called convolution. The principal aim of convolution is that the CNN will learn feature detectors that triggered when they detected certain visual patterns on the input image. Usually, a CNN includes many separate feature detectors and its one of them produces its own feature map [21].

The size of the output is determined by key three factors: the depth, the stride and the pad.

- Depth, describes the number of feature detectors being used in the layer. For instance, when an image is inserted into the CNN many different feature detectors may be activated in the presence of certain patterns.
- Stride is referring to the sliding rate of the feature detector. When stride s is 1, the feature detector is convolved with the image at every practicable spatial location moving from pixel to pixel. On the other hand, when the stride is $s > 1$ every movement of the detector skips $s - 1$ pixel positions [17, Ch. 6.1, pp. 6].
- Pads are used in cases when the size of the input and the output should be equal. If the input is $H^l \times W^l \times D^l$ and the output $H \times W \times D^l \times D$ the convolution result has size $(H^l - H + 1) \times (W^l - W + 1) \times D D$. For every channel of the input if a pad of $\lfloor \frac{H-1}{2} \rfloor$ rows is inserted above the first row, a pad of $\lfloor \frac{H}{2} \rfloor$ is inserted above the last row and the columns $\lfloor \frac{W-1}{2} \rfloor$ to the left of the first column and $\lfloor \frac{W}{2} \rfloor$ to the last column of input, the convolution output will have a size of $H^l \times W^l \times D$. Often, the

element values of the pads are 0. In this case, the process is called zero padding [10, Ch. 6.1, pp. 5].

A distinct example of the convolution process is stated in figure 2.

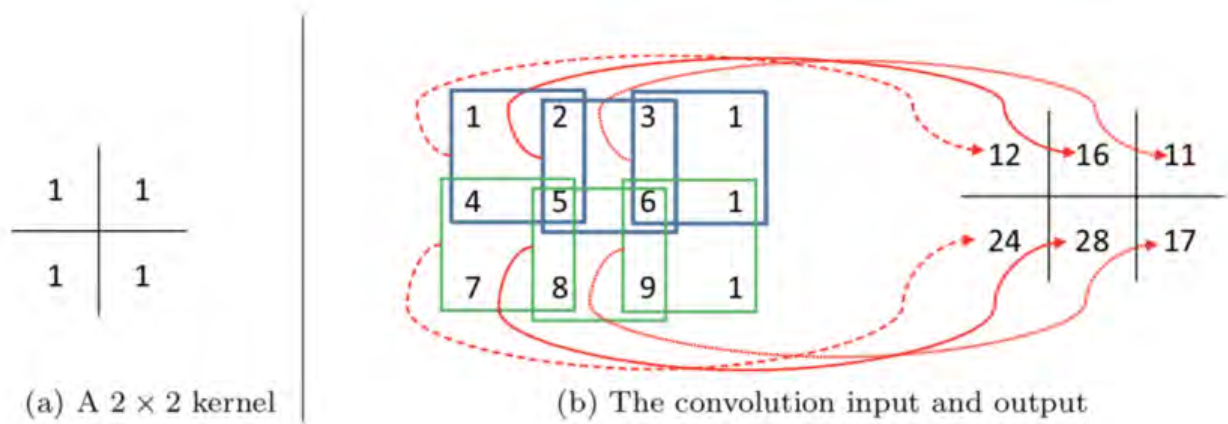


Figure 2: Illustration of the convolution process. Showcased above, the feature detector (kernel) is overlapped with the right top corner area in the input image. The convolution result would be $1 \times 1 + 1 \times 4 + 1 \times 2 + 1 \times 5 = 12$. Then the filter is moved to the next pixel which will give a convolution result of 16 and the operation continues until the filter has slid through all the input's pixels. [17]

3.1.8 Why convolute?

If bias is added to the convolution process, the convolution product can be positive at horizontal edges in a certain direction and negative at different areas. If the next layer in the CNN's design is a ReLU layer, the output of that layer defines many "edge detection features" which activate only at horizontal or vertical edges in certain directions. During the continuation of the forward run into the CNN's deeper layers, the following layers will be able to activate when more specific and complex patterns are found [17, Ch. 6.2, pp. 2]. Moreover, all spatial areas of the input image share the same feature detectors leading to a significant reduction of the parameters needed for a convolution layer. For instance, if the input image contains multiple cats, the "cat-shaped ears" feature detector will be triggered at every cat [17, Ch. 6.2, pp. 3]. Furthermore, on deep CNN architectures convolution allows parameters sharing. For example, the CNN does not need dedicated feature detectors for

“cat-shaped ears” and “dog-shaped ears” in order to detect a dog. It is able maybe to have an “animal fur” detector which can be shared for both occasions [17, Ch. 6.2, pp. 4]. Last but not least, feature detectors like the aforementioned are extremely intuitive. In many cases, the activation may happen for pixels that correspond to patterns that are not related to something as semantic as cat ears [17, Ch. 6.2, pp. 5].

3.1.9 Fully connected layer

Finally, a fully connected layer is the layer that in order to compute its output product x^{l+1} needs all the elements of x^l input. Commonly, fully connected are the very last layers of a CNN’s architecture which are responsible for class labeling and therefore they require all the previous features.

3.2 From Sliding Windows to Mask R-CNN

3.2.1 Sliding-window detectors

Since 2012, when AlexNet designed by Alex Krizhevsky dominated the ImageNet LSVRC-2012 competition, CNNs have ruled the field as the major deep learning method in image classification. Hence, one brute force approach for an image recognition task would be to slide windows all over the image’s surfaces. In order for our detection to be scale-free, windows of varied sizes and aspect ratios should be used. In practice, this means that fractures of the main image are constantly taken and delivered towards the CNN classifier to extract features. Then SVM classification and linear regression are applied for class identification and boundary box designation respectively [8]. Despite the simple concept, sliding-window detectors computational cost is massive. Decreasing the window’s number decreases run-time speed and system resources used, only crucially restraining classification’s accuracy.

3.2.2 Selective Search

Instead of a brute force approach, a region proposal method can be used to create Regions of Interest (ROIs) for object detection.

In selective search (SS) hierarchical groups of similar regions are computed, based on color, texture, size and shape. The architecture of SS is noted in figure 3.

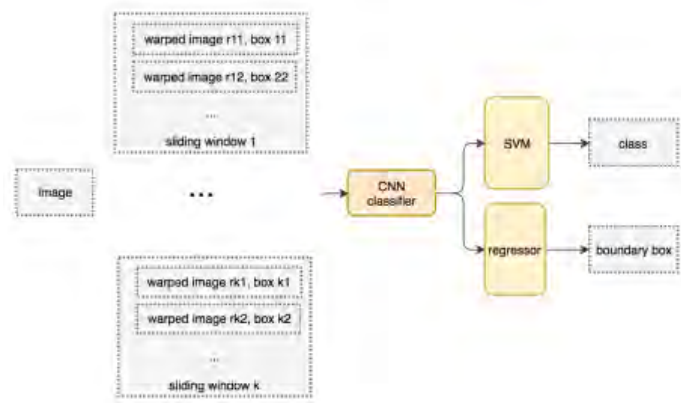


Figure 3: System flow for the sliding-window detector [22]

3.2.3 Pooling layer

An early challenge that needs to be confronted when dealing with an object detection task are differences in scaling and aspect. The object of interest can appear in many forms and sizes into an image, still, it should be correctly identified and classified. In a more abstract approach, this means that if the distinct features of the classified object are a bit distorted the neural network should have some level of flexibility so as to identify these features. In terms of how a CNN works, the prospect of pooling layers is to obtain spatial invariance by reducing the resolution of the feature map which is essentially the distinct features. The resulted pool feature map resembles a feature map of the previous layer. Its units are the input from a small $n \times n$ patch, as indicated in figure 4. This pooling window's size can be arbitrary and windows are allowed to overlap [23, Ch. 3, pp. 3].

An example of max pooling operation is given in Figure 4.

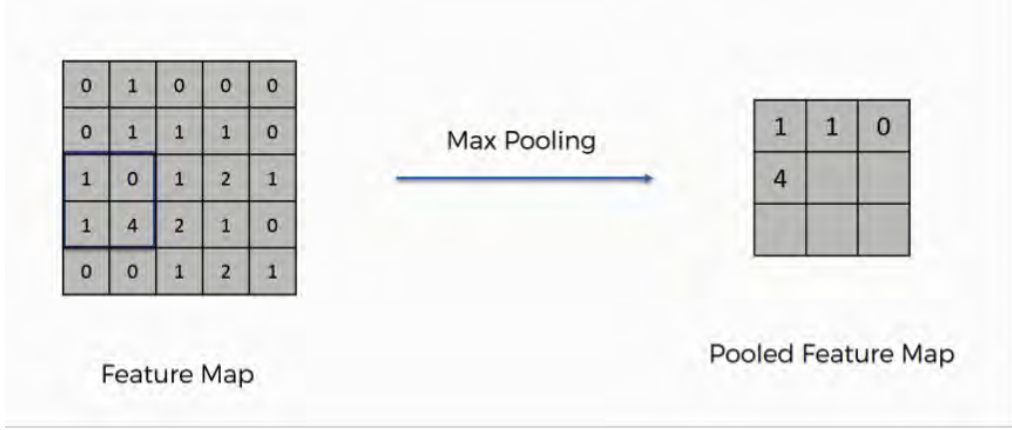


Figure 4: Max pooling with 2×2 pooling window. In this case, we lose 75% of the initial information located on the feature map since the pooled feature map contains only 1 out of 4 original pixels. This information is unnecessary and without which the CNN is more efficient. [24].

Usually, two sorts of pooling methods are applied: max pooling and average or mean pooling. In max pooling, the maximum unit included in the pooling window is transferred to the pooling map, while in mean pooling the mean value of the combined units is transferred instead [17, ch. 7]. In precise mathematics:

$$\text{max: } y_i^{l+1}, j^{l+1}, d = \max_{0 \leq i < H, 0 \leq i < W} (x_{i^{l+1} \times H + i, j^{l+1} \times W + j}^l, d),$$

$$\text{average: } y_i^{l+1}, j^{l+1}, d = \frac{1}{HW} \sum_{0 \leq i < H, 0 \leq i < W} x_{i^{l+1} \times H + i, j^{l+1} \times W + j}^l, d,$$

Equations 8a, 8b: Max and average pooling

As a result, the CNN is now able to account for distortions. This process is what provides the network with the aforementioned spatial variance capability. Besides that, pooling assists in minimizing the images' size as well as the number of parameters, a result that eventually prevents overfitting from coming up.

3.2.4 Fast R-CNN

After SS, Fast R-CNN algorithm appear. This architecture uses a region proposal method to construct around 2000 RoIs. The regions are removed from the original image and enter into a CNN for classification. Even though this method achieves an excellent detection accuracy in lesser time than SS, R-CNNs are still impractical in terms of training and object detection speed [22].

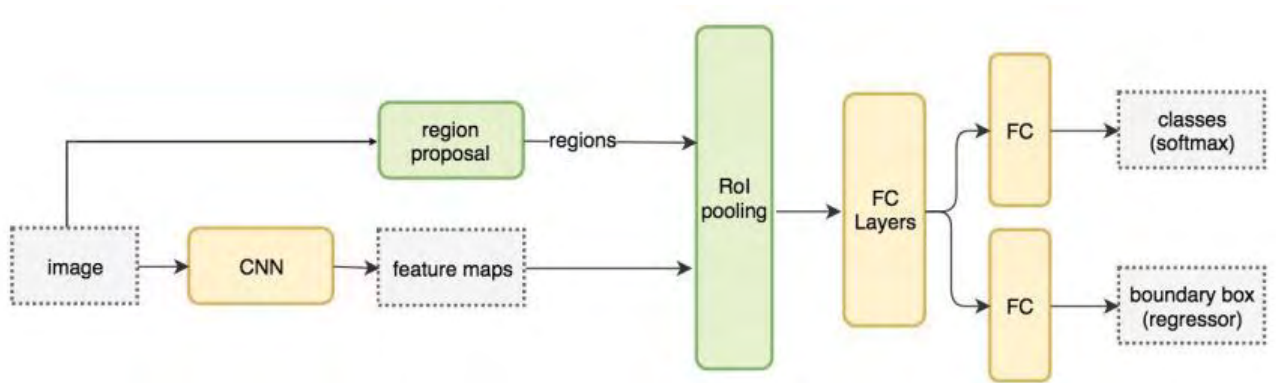


Figure 5: Workflow of a fast R-CNN [22]

3.2.5 RoI Pooling

RoI pooling is a neural net layer using max pooling to turn the features included into a valid RoI area to a small feature map with a determined spatial extent of $H \times W$ [25, Ch. 2.1, pp. 1]. The layer takes two inputs:

- A fixed-size feature map gathered by a CNN with numerous convolutions and max pooling layers.
- A RoI feature map.

For every RoI of the input list, RoI pooling takes a section of the input feature map that corresponds to it and scales it down to a pre-setted size. The scaling is done by dividing the $h \times w$ into an $H \times W$ grid of equal-sized parts. The size of the parts is $h/H \times w/w$. Then max pooling is applied to the windows the output units are transferred to the corresponding output

grid cell [25, Ch. 2.1, pp. 1]. The result is that starting from a group of rectangles with several sizes, a list of corresponding fixed size feature maps is generated. Note that the dimension of the corresponding pooling feature map depends only on the number of sections the proposal is divided into and not on the region proposals and feature maps sizes. Finally, the main reason we need ROI layer is speed. Usually, there are many region proposals on the frame, yet the network is still able to use the same feature map for every one of them [26].

3.2.6 Faster R-CNN

A year after the Fast R-CNN deployment, a small team of researchers, including Ross Girshick, replace the selective search external region proposal method with a new internal deep network called RPN and can be seen in figure 6. This design change meant that RoIs are now produced by feature maps and manage to diminish the time needed for RoIs generation from 2 seconds to 10 ms [22].

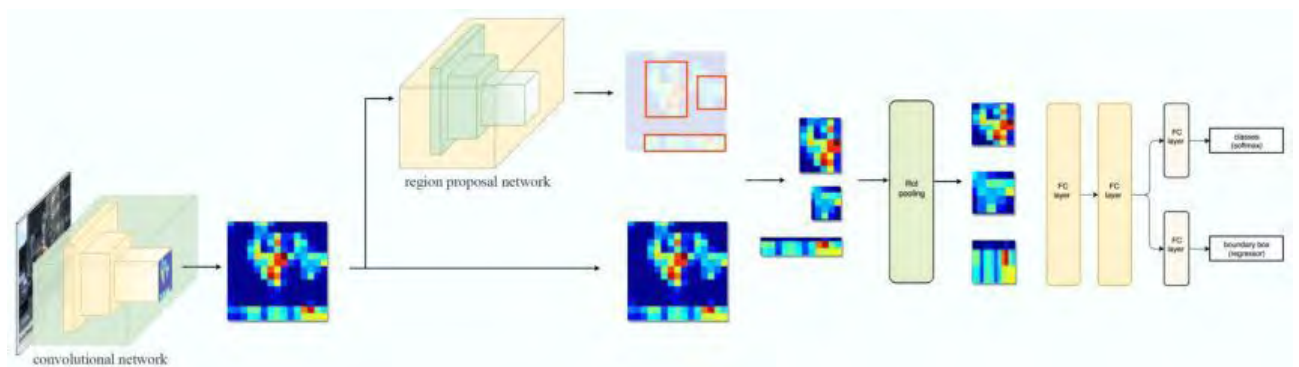


Figure 6: *Faster R-CNN architecture. Fast and Faster R-CNNs share the same work main design. The only notable variation is the way region proposals are generated [22]*

3.2.7 Region Proposal Networks

According to Shaoqing Ren et. al, an RPN takes an image (of any size) as input and outputs a set of rectangular object proposals, each with an objectness score. Objectness primarily suggests membership measurement to a set of object classes versus background [26, Ch. 3,

pp. 1]. RPN consists a box-classifier which ascertains the probability of the proposal describes the target object and a box-regressor for determining the coordinates of the proposals. Instead of using pyramids of filters, RPN applies novel “anchor” boxes. For proposal generation, a small network is slid over the outputted convolutional feature map by the last shared convolutional layer. An $n \times n$ spatial window of the input convolutional feature map is fed to the small network, while its sliding window is mapped to a lower-dimensional feature. Lastly, the box-classification and the box-regression layers take as input this feature map [26, Ch. 3, pp. 2]. The RPN integration into faster R-CNN architecture is given figure 7a while the workflow of the algorithm is demonstrated in figure 7b.

Anchors

At each sliding window location, multiple region proposals are predicted simultaneously, where the number of maximum proposals for each location is indicated as k . Thus, the regression layer has $4k$ outputs encoding the coordinates of k boxes, and the classification layer has $2k$ scores that predict the probability of a proposal being an object or not. The k proposals are parameterized relative to k reference boxes which called anchors. An anchor is centered at the sliding window in question and is linked to a scale and aspect ratio. The developers of RPN architecture choose 3 scales and 3 aspect ratios, generating $k = 9$ anchors at each sliding position. Given a convolutional feature map sized $W \times H$, the estimated number of anchors is $W \times H \times k$ [26, Ch. 3.1].

Label Assignment and Loss Function

During the training step, a binary class label (being an object or not) is assigned to each anchor. A positive label is attached to two sorts of anchors (Note that a ground truth box may allow positive labels to multiple anchors):

- The anchors with the highest IoU overlap with a ground a ground-truth box
- An anchor having IoU overlap higher than 0.7 with any ground truth box

On the other hand, negative labels are assigned to anchors having an IoU ration lower than 0.3 for every ground truth box. Last but not least, anchors that are not labeled as positive or negative have zero contribution to the training process [26, Ch 3.1.2, pp 1].

Conclusively, since this is a training process a loss function needs to be minimized. RCN loss function for an image is defined as:

$$\text{Loss function: } L(\{p_i\}, \{t_i\}) = \frac{1}{N_{cls}} \sum_i L_{cls}(p_i, p_i^*) + \lambda \frac{1}{N_{cls}} \sum_i p_i^* L_{reg}(t_i, t_i^*),$$

Equation 9: RCN loss function

where i is the index of an anchor in a mini-batch, p_i is the predicted probability of anchor i being an object. The ground-truth label p_i^* has a value of 1 if the anchor is positive, and a value of 0 if the anchor is negative. t_i is the vector of 4 coordinates of the bounding box (top left corner coordinates, height, width) and t_i^* is that of the ground-truth box linked to a positive anchor [26, Ch. 3.1.2, pp 2].

The classification loss L_{cls} is log loss across two classes (being an object or not). The regression loss is calculated using $L_{reg}(t_i, t_i^*) = R(t_i - t_i^*)$, where R corresponds to the robust loss function:

$$smooth_{L_1}(x) = 0.5x^2 \text{ if } |x| < 1 \text{ and } smooth_{L_1}(x) = |x| - 0.5 \text{ otherwise.}$$

Equation 10: $smooth_{L_1}(x)$

The term $p_i^* L_{reg}$ suggests that the regression loss function is triggered only for positive anchors $p_i^* = 1$ and is deactivated otherwise $p_i^* = 0$. The products of the regression and classification layers consist of $\{p_i\}$ and $\{t_i\}$ respectively [26, Ch. 3.1.2, pp. 2].

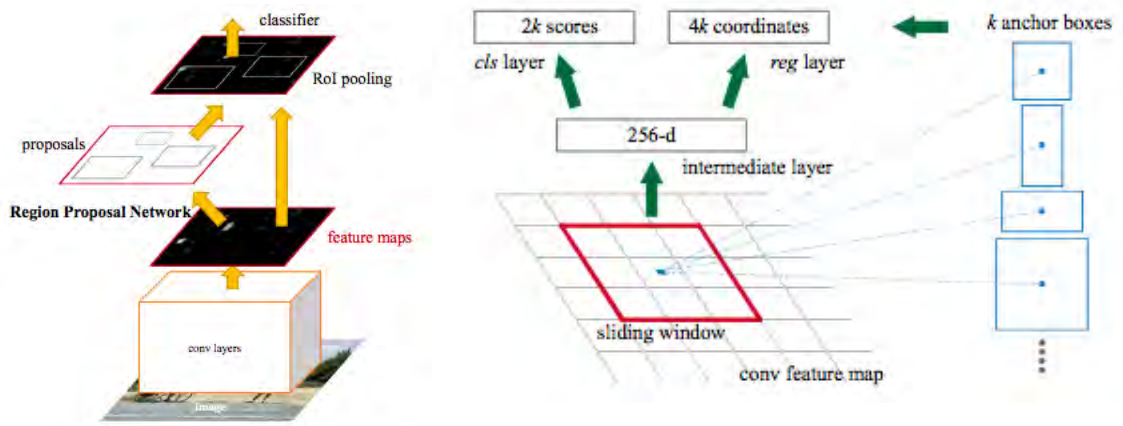


Figure 7a: *Faster R-CNN workflow with RPN usage highlighted*[27], Figure 7b: *Region proposal network workflow* [27].

3.2.8 Mask R-CNN

As the name suggests, mask R-CNN is a continuation of the earlier R-CNN variations and developed in 2017 by the FAIR team. Mask R-CNN uses Faster R-CNN as a blueprint and extends its design by aiming to locate exact pixels of an object instead of only highlighting it with a bounty box [28]. This operation in the computer vision world is called segmentation. As is demonstrated in figure 8, a special branch is being added that generates a binary mask determining if the given pixels are part of the target objects or not. Yet, the original Faster R-CNN architecture needs a supplementary adjustment since regions of the feature map selected by RoI pooling were misaligned compared to the regions of the primary image leading to inaccurate pixel masks. To bypass this issue, the FAIR team researchers re-engineered the RoI polling operation in a different manner. They replace quantization of the ROI boundaries with the use of bipolar interpolation to calculate the exact values of the input features at four regularly sampled locations [20]. In simpler terms, given a 256×256 image as an input and having a 25×25 feature map, if a 16×16 pixels RoI is proposed, means that the corresponding feature to original ratio is $25/256$. For the previous case, RoI is translated to $16 \times 25/256 = 1.56$ pixels. In the case of Faster R-CNN, this value would be rounded to 1 and consequently lead to misalignment. Instead in Mask R-CNN, the exact value can be kept. This process is highlighted in Figure 8.

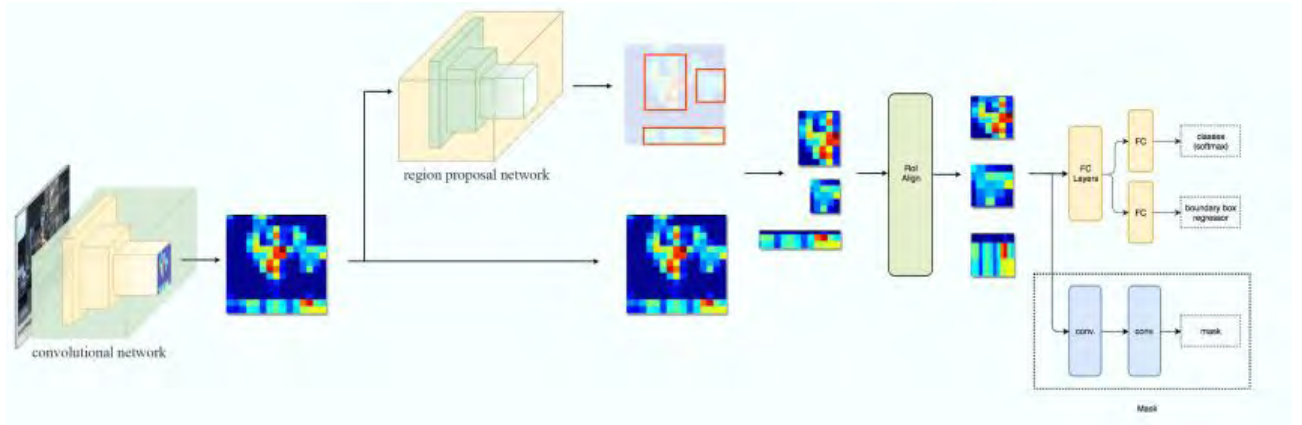


Figure 8: Mask R-CNN architecture. Its implementation adds an additional branch dedicated to binary mask generation [20].

4. ANNUAL ENERGY YIELD CALCULATION

Trying to estimate the annual energy yield of a solar panel is usually a quite complicated process. The concept of harnessing solar energy in order to generate electricity is only possible thanks to the solar radiation phenomenon. Hence, annual solar radiation data needs to be collected corresponding to the coordinates of the location that the PV system is about to be installed. Moreover, the system's orientation is crucial for the final power production, since solar panels should face true south for maximum power production and other orientation could cause losses. In cases where the solar installation would happen on fixed pre-existing surfaces such as rooftops, the roof's angle must be measured. Shading is essential too. Then, there is module's efficiency based on several additional factory specifications, while the local temperature is also significant. Last but not least, system losses should be considered. There are many equations, models and software that address this challenge. An intuitive equation that can be used as first step is given below:

$$E = A \times r \times H \times PR$$

Equation 11: *Annual energy yield estimation*

where E is the annual energy (KWh), A is the total solar panel area (m^2), r is the panel's efficiency (%), H is the annual average solar radiation W/m^2 and finally PR is the performance ratio, a metric which integrates the systems losses [30]. Figure 9 presents the nature of energy losses among PV systems, while a stepwise approach of annual yield estimation is displayed at figure 10.



Figure 9: *Energy production losses* [29]

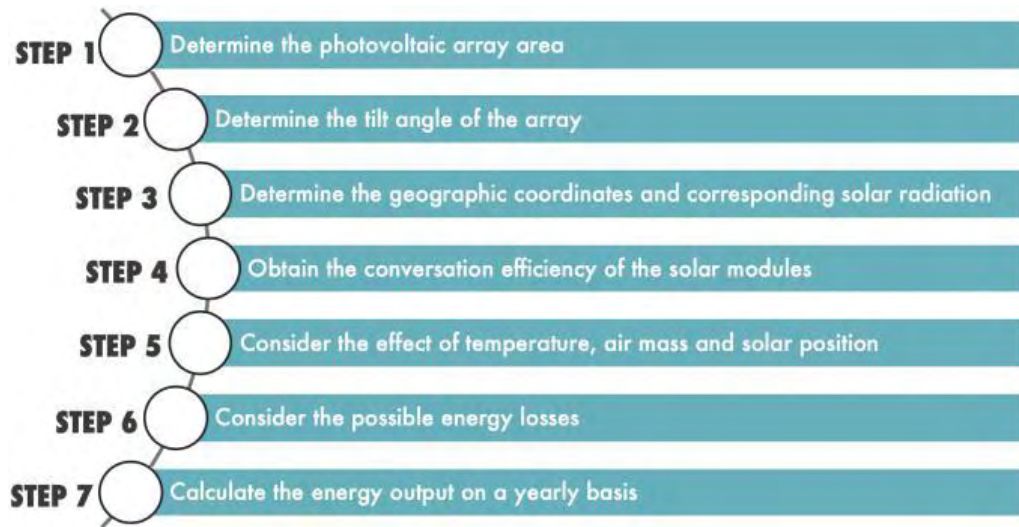


Figure 10: A stepwise approach in annual energy yield calculation

4.2 The effect of physical phenomena

4.2.1 Air Mass

According to Matthew J. Reno et. al [31] in solar energy air mass (AM) actually refers to the relative air mass that is measured in relation to the path length at the zenith. For instance, $AM = 0$ indicates the absence of atmosphere and terrestrial radiation is equal to the extraterrestrial one while $AM = 1$ means that the sun is positioned right above. This physical phenomenon explains why the colors of the objects located near the horizon are significantly faded in comparison to object's colors that are directly overhead [31]. Additionally, AM affects solar spectrum and causes refraction of the sunlight, an effect that leads into lengthier paths. For PV installations, $AM = 1.5$ is the optimal value.

4.2.2 Solar Position

The solar energy that reaches earth's surface is extremely correlated with the sun's position in the sky. The lesser the zenith angle, the shorter the layers of the atmosphere are [31].

During the so-called solar noon, which occurs when the sun crosses the meridian on either the spring or fall equinox, the zenith angle z is equal to the latitude of the location ϕ :

$$z = \phi$$

Equation 12: *Zenith angle calculation during solar noon.*

Otherwise, z is calculated by subtracting the declination angle δ :

$$z = \phi - \delta$$

Equation 13: *Alternative zenith angle formula.*

where $\delta = 23.45\sin(x)$, with $x = \frac{360^\circ}{365}(DOI - 81)$. Solar position is a crucial worth considering factor during the installation process in order to accurately model PV system performance.

4.2.3 Solar radiation

Solar radiation can be the core of solar energy. Namely, the sun's energy is produced by an endless nuclear fission reaction during which 700 million tons of hydrogen are converted to helium per second [32]. Due to this process, enormous amounts of heat are generated in the sun's surface, causing the release of photons which after a long journey are able to reach outer space and in our case Earth's atmosphere in the form of extraterrestrial radiation E_a :

$$E_a = E_{sc} \times \left(\frac{R_{av}}{R}\right)^2$$

Equation 14: Extraterrestrial radiation.

where E_{sc} is the solar constant 1376 W/m^2 , R_{av} is the mean sun-earth distance and R is the actual sun-earth distance depending on the day of the year which varies due to earth's elliptical orbit [26].

Even on a cloudless day however, a portion of the E_a is scattered and absorbed as it passes through the atmosphere. It is estimated that on a clear day at noon only 75% of the E_a reaches the ground, a fraction that is further decreased during morning and evening hours [31]. The radiation springing straight from the sun is named direct normal irradiance (DNI) and is measured as the amount of solar radiation received per unit by a given surface that is always held perpendicular to the direction of the sun [33]. On the other hand, the radiation that is scattered through the atmosphere diverges randomly in every direction. Thus, a portion of this radiation is redirected towards the earth's surface and is called diffuse horizontal irradiance (DHI). DHI is actually the reason why there is light in shady places and the sky is bright during daytime [31]. Through overcast days DHI is the main source of solar power. Furthermore, sunlight reflections from the ground contribute to the total portion of DHI. The amount of terrestrial radiation falling on a horizontal surface is the global horizontal irradiance (GHI) and is the sum of DHI and DNI when projected into the horizontal surface:

$$GHI = DHI + DNI \times \cos(z)$$

Equation 15: *Global Horizontal Irradiance*

where z is the solar zenith angle [33]. The knowledge of GHI is mandatory for the PV power output calculation.

4.2.4 Temperature

Local temperature can affect solar panels' efficiency. During production, every PV module is going through a series of tests before it makes its way into the market. The temperature in these lab conditions is 25° [34] which is considered to be the ambient temperature. As the temperature of the solar panels rises, its output current increases exponentially while the

voltage output linearly decreases, leading to a severe reduction in the PV module's power production.

Thus, solar panel manufacturers provide the so-called temperature coefficient, a term that quantifies the module's heat tolerance by describing how much power the module will lose when a temperature increment by 1° is occurring [35]. For instance, if a 150 W solar panel has a temperature coefficient of $-0.32\%/C$, operating at 35° , the power output reduction would be $150W \times (30^\circ - 10^\circ) \times (-0.32\%/C) = -4.8W$. Thus, the real power output, in this case, is 145.2 W. On the other hand, it is obvious that for temperatures below the ambient the power output is greater. For example, if the aforementioned module was operating at 15° the real power output would be 154.8 W.

5. METHODOLOGY

5.1 Overview

In this section, we aim to describe the process followed in our research, including our assumptions, tools and model cases. This study can be split into two big parts: the use of computer vision techniques and algorithms for rooftop detection on satellite imagery and the modeling of photovoltaic production throughout the years. In order to comprehensively explore, analyze and assess the multi-dimensional aspects of this approach, programming in Python language, Mask R-CNN and PVvlib were employed as the main tools for this thesis. As a starter point, Mask R-CNN computer vision algorithm is used to detect and extract available areas for photovoltaic panel installation and, specifically, rooftops. This algorithm was the optimum option for image segmentation in not only detecting the desired object but also separating it from its surroundings, allowing us to calculate its exact dimensions, orientation and positioning on the global map. From that point and onwards, Python's Pvlib library is used to simulate the installation and calculate the optimum parameters to be used, like the type and model of solar panels and inverter that suit a specific case. To better demonstrate the results of our research, we examined two separate cases with different characteristics and demands: a medium-sized, residential, south-oriented building and a large, commercial, north-oriented building.

5.2 Image loading

The first step for implementing the software requirements is finding an elegant and easy way of accessing satellite imagery. Thus, the Maps Static API is used so as to load images based on the geographic coordinates of the location of interest. The Maps Static API is a member of the Google Maps Platform, a software service developed from Google specifically for allowing Google Maps integration into third-party applications. Apart from the location's longitude and latitude, a zoom level has to be specified along with the output image dimensions and format. The zoom level corresponds to the vertical distance which an external observer sees the earth surface. Table 2 demonstrates the magnitude of the zoom level. For instance, zoom level set to 0, will result in an image containing the whole earth.

Therefore, for this implementation, a zoom level of 19 is used, allowing the representation of individual buildings. The generated images are chosen to have a jpeg format.

In order to be able to convert the number of pixels corresponding to a rooftop to square meters, the square meter per pixel ration needs to be calculated for the respected zoom level and location. According to Chris Broadfoot, one of Google’s employees, the conversion equation is the following:

$$Meters/Pixel = 156543.03392 \times \cos(latitude \times \pi/180)/2^{zoomlevel}$$

Equation 16: *Meters per pixel ratio*

The abovementioned equation is based on the assumption that the earth’s radius is 6378137 m [36]. As a result, the rooftop’s surface is:

$$surface = pixels \times (Meters/pixel)^2$$

Equation 17: *Rooftop’s acreage.*

where “pixels” is the number of pixels corresponding to a rooftop.

Information regarding zoom levels:

Level	Number of Tiles	Tile width (° of longitudes)	m/pixel (on Equator)	Scale (on screen)	Examples of areas to represent
0	1	360	156 412	1:500 million	Whole world
1	4	180	78 206	1:250 million	
2	16	90	39 103	1:150 million	Subcontinental area
3	64	45	19 551	1:70 million	Largest country
4	256	22.5	9 776	1:35 million	
5	1,024	11.25	4 888	1:15 million	Large African country
6	4,096	5.625	2 444	1:10 million	Large European country

7	16,384	2.813	1 222	1:4 million	Small country, US state
8	65,536	1.406	610.984	1:2 million	
9	262,144	0.703	305.492	1:1 million	Wide area, large metropolitan area
10	1,048,576	0.352	152.746	1:500 thousand	Metropolitan area
11	4,194,304	0.176	76.373	1:250 thousand	City
12	16,777,216	0.088	38.187	1:150 thousand	Town, or city district
13	67,108,864	0.044	19.093	1:70 thousand	Village, or suburb
14	268,435,456	0.022	9.547	1:35 thousand	
15	1,073,741,824	0.011	4.773	1:15 thousand	Small road
16	4,294,967,296	0.005	2.387	1:8 thousand	Street
17	17,179,869,184	0.003	1.193	1:4 thousand	Block, park, addresses
18	68,719,476,36	0.001	0.596	1:2 thousand	Some buildings, trees
19	274,877,906,944	0.0005	0.298	1:1 thousand	Local highway and crossing details

Table 2: Information regarding zoom levels. The number of tiles column refers to the portion of tiles needed to represent the entire world. Tile width provides the width of the map in degrees of longitude while m/pixel column highlights how meters are explained by each pixel. This is a rough estimation however and this metric is calculated accurately by equation 16 [37].

5.3 Model Implementation

The next step is the computer vision algorithm. The specifications of this project require not only an accurate recognition of rooftops, given an input image, like the one offered by many boundary box style detectors, but also the grouping of pixels based on whether they belong to a rooftop depiction or not. This is the main reason why Mask R-CNN algorithm was chosen as our final choice for this study.

The implementation of the main algorithm is heavily based on a slightly modified usage of Matterport’s Mask R-CNN build [38], modified by Sharada Prasanna Mohanty for 2018

Crowd AI mapping challenge [39]. Matterport's implementation uses an FPN along with an RPN, for improved feature extraction and ReSNET101 backbone to construct the bottom-up pathway through the pyramid of feature maps. This build was trained on Microsoft COCO library [40]. COCO contains a massive number of datasets tailor to image segmentation purposes, including 1.5 million object instances and more than 200K labeled images within 80 different object categories. Despite the large portion of image classes that COCO contains, none of them corresponds to rooftops. Thus, in the modified version, the main build was altered is so as to be compatible with a conventional training set, using JPEG images.

Applying a mask, however, is not enough since only the number of pixels corresponding to each mask is known. Hence, every time a binary mask is generated, before the visualization process, the mask's surface size is calculated by equation 18 using the estimated meters/pixel ratio for the current location.

5.3.1 Detection

The detection function is the core of the segmentation process. During this step, the calculation of the ROIs, scores (the probabilities of an ROI being a rooftop or not), binary masks and mask's acreage are occurring. The detection process as a whole is can be seen in Figure 11, on the following page.

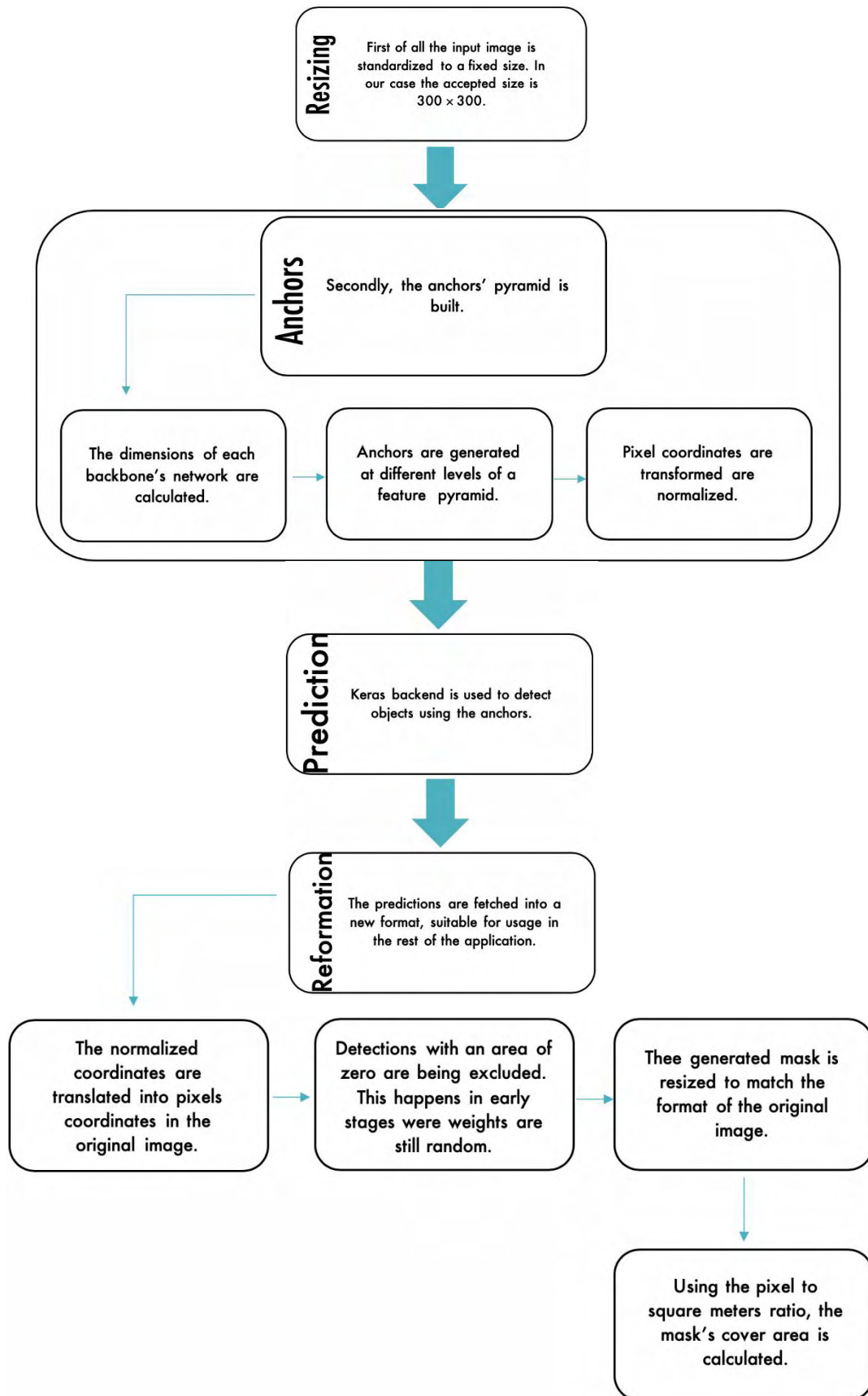


Figure 11: Flowchart of the detection process

5.3.2 Visualization

The next step is to apply the predictions visually into the input image. For every ROI, the corresponding boundary box, the score and the binary mask need visualization. Since the coordinates of the spatial instances are already known, plotting is a fast and easy process. Its variable is added to the original image an order similar to the detection process. A demonstration of the whole visualization step is given below, in Figures 12a-12f. Keep in mind that this is the exact same order that variables being are estimated during the detection step.



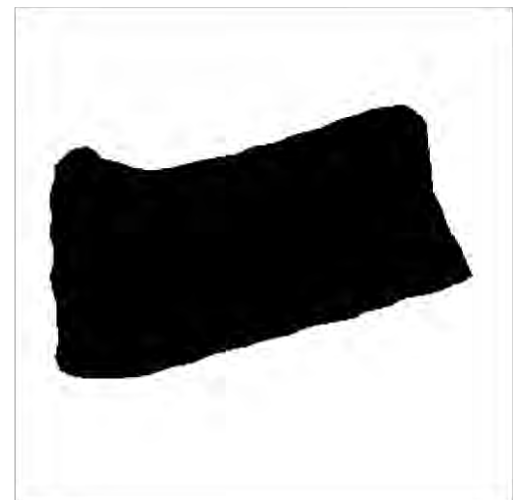
(a)



(b)



(c)



(d)



(e)



(f)

Figures 12a -12f: *Demonstration of the detection and visualization process*

- a - An input satellite image.
- b - The boundary box is being deployed based on the anchors.
- c - The probability that the boundary box contains a building is calculated.
- d - The binary mask is generated and the corresponding acreage is measured.
- e - The binary mask is applied to the output image.
- f - Final result.

5.4 Model Training and Evaluation

5.4.1 Training using two distinct datasets

The training process can be quite challenging in computer vision tasks. One of the main challenges that needs to be addressed is the distinct diversity that occurs in terms of rooftop sizes, shapes and colors. In the case of the Netherlands, many residential buildings have tile roofs, while more modern structures may have concrete ones. Moreover, large industrial

buildings like factories, etc. are usually built with metal rooftops., so this instance needs to be covered as well. Additionally, the model should have the flexibility to distinguish a rooftop in every possible pattern variation. It is obvious for example, that a shift in scenery occurs in the transition from an urban to a woodland environment. In order to cover all these discrete scenarios, the training set is required to include a vast portion of respected images corresponding to each individual case.

Two different training sets were used during this project. Firstly, a fixed data set is used, containing 3000 satellite images from various buildings at 19 zoom level. In this imagery set, about 1000 satellite images of Dutch buildings were added with the hope that eventually the algorithm's would become more specialized in the Dutch architecture. Moreover, an image generation algorithm was applied in order to further increase the training image sample. With the usage of a process similar to CNN's, realistic representations of satellite images are generated by picking random noise from the training set and then through backpropagation and weight adjustment, altering the original design until it reaches an accepted similarity level compared with the original training set. This process adds 1000 additional AI produced images. Then, the dataset is split into the training set and the test set using a 0.7 split ratio. For the deployment of this model, Google Cloud Compute virtual machine was used since the computational power required for this task is quite extensive. Secondly, for the training process, a dataset provided by CrowdAi [41] is used, consist of 341,058 rooftop satellite images. Finally the dataset is split between a training test of 280,741 images and a test set of 60,317 images, used to first train the model and then assess it accuracy.

5.4.2 Evaluation Process

In order to be able to precisely evaluate the model's performance, daftlogic's google map area calculator software is used. This software estimates the measurements of enclosed areas that are designated using a drawing tool. To better access the model's efficiency, the tested buildings are grouped by whether they are residential or commercial and if their location is beneath an urban area or the countryside. Then the margin of error is calculated using the equation 18:

$$error = | estimated - real | (m^2)$$

Equation 18: *Margin of error*

where estimated is the output area measurement and real is the measurement calculated by the external tool. The accuracy of its prediction is:

$$accuracy = 100 - \frac{error}{real}$$

Equation 19: *Prediction accuracy*

5.5 Photovoltaic system modeling

5.5.1 Pvlib python

Pvlib python is an open source tool, developed on GitHub by contributors from different backgrounds in the field of renewable energy. It is heavily based on its pvlib Matlab sibling toolbox created at Sandia National Laboratories and is intended to simulate the performance of photovoltaic energy systems [43]. The structure of the toolbox consists of three core classes: Location, PVSystem and ModelChain. A Location object represents a real place across the globe while a PVSystem object models an assembled group of solar panels, inverters, etc. Also in this step, various models that explain physical phenomena like solar radiation, solar position, air mass, etc. need to be configured. Finally, the ModelChain class serves as a mean for calculating the PVSystem energy output in a given location [44].

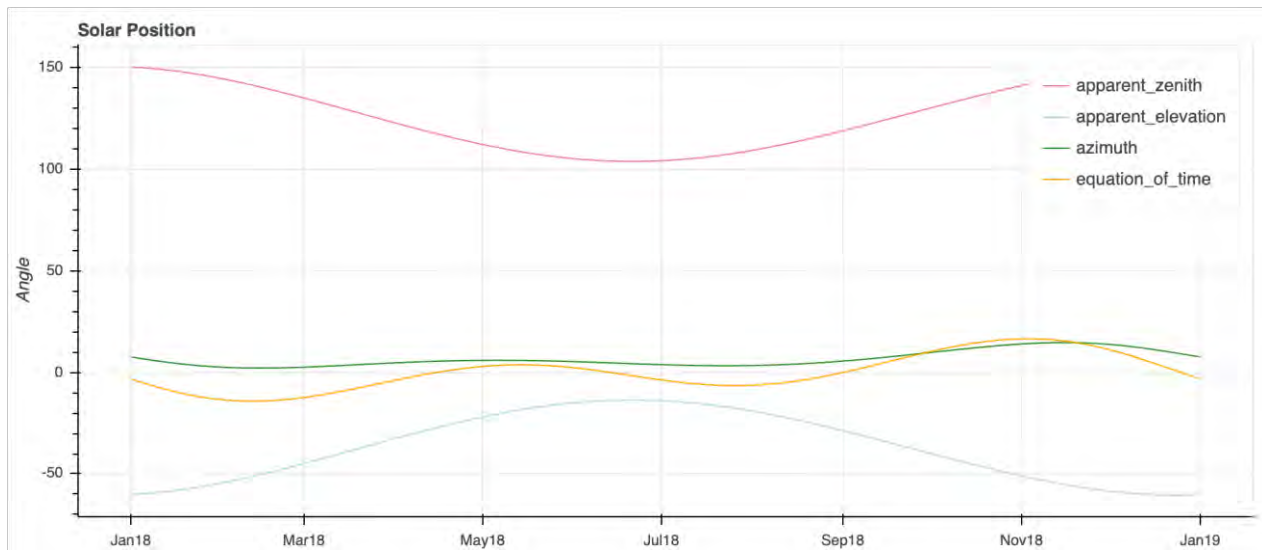
5.5.2 Modeling Air Mass and Solar Position

Kasten and Young (1989) AM model is used in the annual energy yield forecasting process. The Kasten and Young model is given below:

$$AM = \frac{1}{\cos(z) + 0.50572(76.07995 - z)^{-1.6354}}$$

Equation 20: *Kasten and Young air mass model*

The solar position is determined using NREL’s Solar Position Algorithm (SPA). SPA is an algorithm developed in 2004 and forecasts the solar position with extreme accuracy for the years -2000 to 6000 based on a combination of date, time and location [45]. Azimuth and zenith angles along with the sun’s elevation and the equation of time are demonstrated for the annual year 2018 in graph 7.



Graph 6: Azimuth, zenith angles, solar elevation and equation of time for the Amsterdam region in 2018.

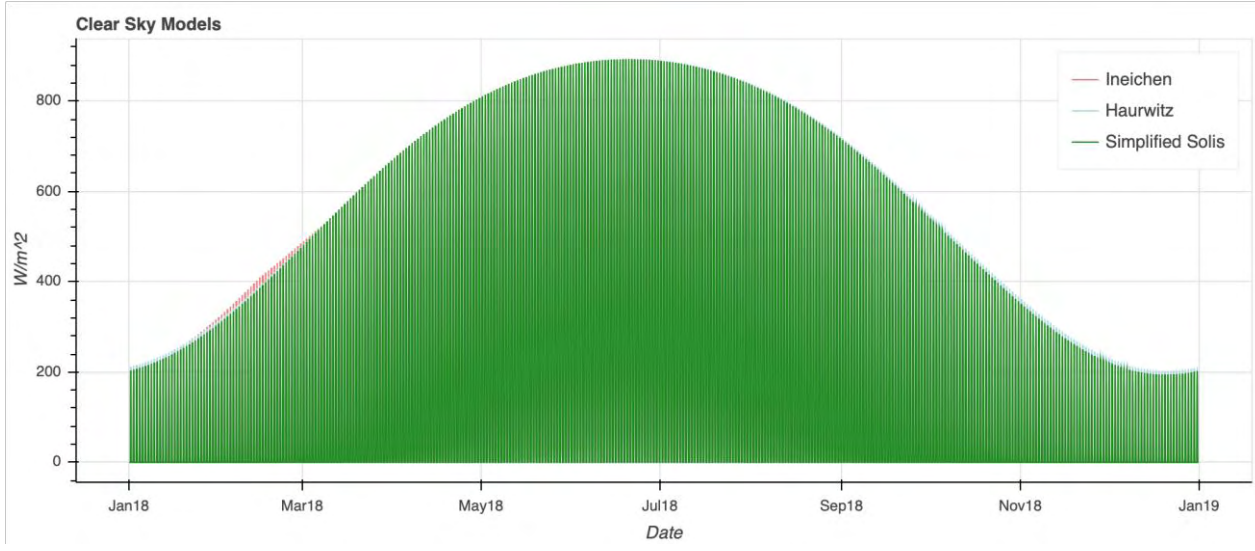
5.5.3 Solar Radiation Models

Equation 16 is a rather simplified and empirical approach to modeling solar radiation. Pvlib models GHI using a clear sky model. The available models are Ineichen and Perez (2002), B. Haurwitz (1946) and Simplified Solis (2008). Graph 8 compares the GHI estimations for the year 2018 made by all three models. Judging by the resulted graph, it is clear that the estimations deviation between the respected models is insignificant. Hence, the Ineichen and Perez clear sky model is being chosen, since it provides the simplest approach in terms of external parameters. Ineichen and Perez model was an extension of the Kasten equation that was proposed in 1984 [31]. The equation that measures GHI is noted below:

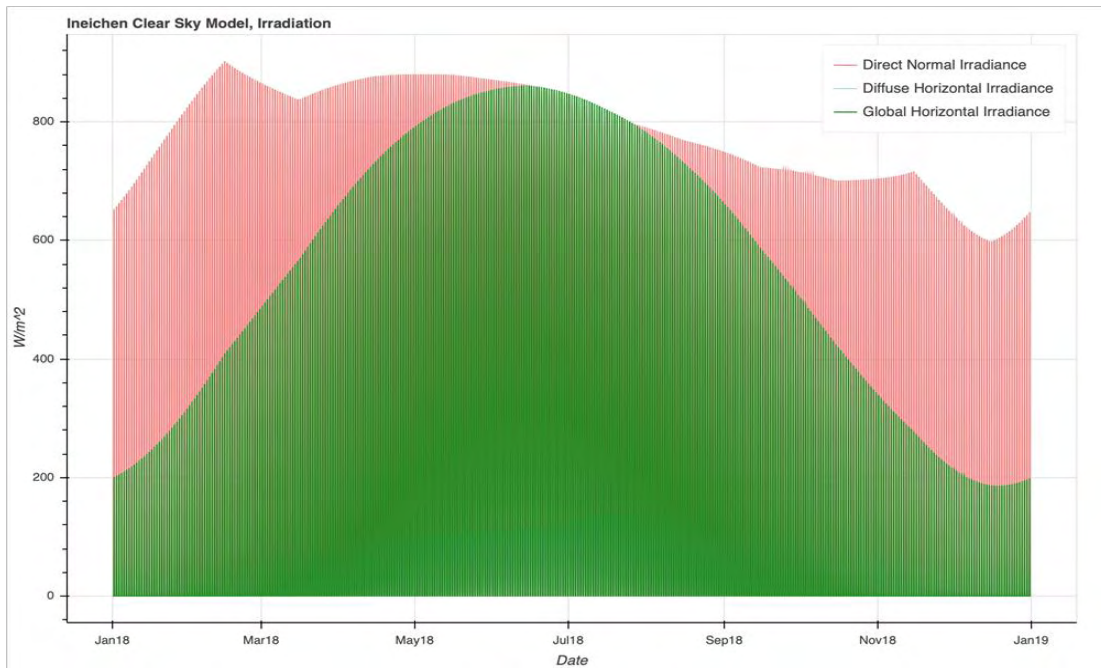
$$GHI = c_{g1} \times \cos(z) \times \exp(-c_{g2} \times AM \times (f_{h1} + f_{h2}(TL - 1)))$$

Equation 21: Ineichen and Perez mode

where $c_{g1} = 5.09 \times 10^{-5} \times h + 0.868$, $c_{g2} = 3.92 \times 10^{-5} \times h + 0.0387$ and h is the elevation. The products of Ineichen and Perez formula are demonstrated in graph 9.



Graph 7: Comparison of the clear sky models available in pvlb.



Graph 8: GHI, DNI and DHI values for the 2018 annual year using Ineichen and Perez clear sky model

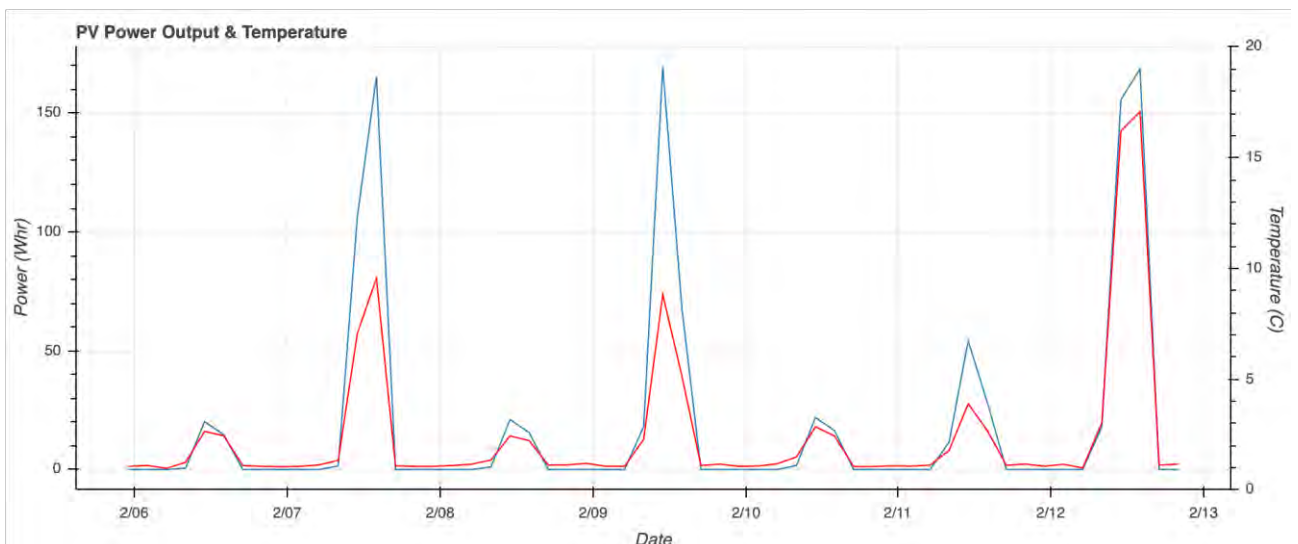
5.5.4 Temperature Model

During the module simulation process, the build-in samp temperature model was used. The next graph demonstrates how power output and module temperature are related. In addition, Table 3 demonstrates the average monthly local temperatures along with the respected average low and max temperatures. In neither of those instances, the local temperature exceeds the ambient one. Therefore, losses related to temperature should not be considered. In reality, the low temperatures of Amsterdam assist power production. The correlation between temperature and PV power output is highlighted in graph 10.

Average monthly temperatures in the region of Amsterdam:

	January	February	March	April	May	June	July	August	September	October	November	December
AVG Temp (°C)	3	4	6	8	12	15	17	17	15	11	7	4
AVG Temp (°C) MIN	1	0	3	4	8	11	13	13	11	8	4	3
AVG Temp (°C) MAX	5	8	9	12	17	19	21	21	18	15	9	6

Table 3: Average monthly temperatures in the region of Amsterdam [31]



Graph 9: PV power output related to temperature

5.6: PV Module and Inverter selection

5.6.1: PV Module Selection

Nowadays, photovoltaic modules are easily accessible and more affordable than ever. Different types of panels are available to serve different needs, at different price ranges. As a result, there are many factors to consider when choosing the optimal photovoltaic module to ensure that the investment will be as profitable as possible in the future.

The main categories of PV panels are:

- Monocrystalline panels: are the most efficient – that is they require the least possible area to install – but they are also the most expensive ones.
- Polycrystalline panels: are less efficient than monocrystalline ones but their price is much more affordable.
- Thin-film panels: are the least expensive ones but they require the largest area to install – about twice as much as monocrystalline panels. Therefore thin-film panels are a good choice only if you have enough area available on your roof.

One thing that is really important in the process of selection, is to make sure that the manufacturer of the panels ensures optimum quality and offers a 25-year guarantee. Bad quality panels can present the Staebler - Wronski effect, in which the efficiency of an amorphous silicon solar cell critically drops during the first six months of operation, typically between 10% and 30% [46].

Despite some recent achievements in thin-film panels production technology, it should be noted that crystalline panels (mono- and poly- ones) are the common type preferred for photovoltaic systems. In our case, we opted for polycrystalline panels, since they have the lowest price per Watt while maintaining their efficiency at quite high levels.

5.6.2: Inverter Selection

A solar inverter (or photovoltaic inverter) is a type of electrical converter which is used for the conversion of the variable DC output(direct current) of a PV module into a utility frequency AC (alternating current), which most appliances use to function. Without a solar inverter, energy harnessed by solar panels cannot be easily put to use, since only alternating current with the correct frequency can be fed into a commercial electrical grid or used by a local, decentralized, off-grid electrical network. It is a critical balance of system (BOS) - component in a PV system installations, making the use of ordinary AC-powered equipment possible and easily doable.

Inverters used in photovoltaic systems are commonly split into the following three categories:

- **Stand-alone inverters:** This type of inverters is used in isolated systems. The inverter draws its DC energy from batteries charged by photovoltaic arrays. Normally, stand-alone inverters do not interface with the utility grid in any way. As a result, islanding does not occur and these systems do not require anti-islanding protection. According to Saleh, Esa et. al. Islanding is the condition in which a distributed generator (DG) continues to power a location even though electrical grid power is no longer present [47]. A great percentage of stand-alone inverters nowadays incorporate internal battery chargers to charge their batteries from an external AC source, when available. This further optimizes the function of the inverter, since it allows for greater savings and autonomy. In this document, we are not going to consider this type of appliance since the case study focuses on grid-tied systems.
- **Grid-tie inverters:** The phase of a grid-tie inverter matches with the supply from utility. It consists of a special circuit used to match the voltage and frequency of the grid, thus enabling the PV panel installation to supply electricity to the grid. Since this type of inverters is directly tied to the grid, the danger of islanding is present and thus it is mandatory for the system to be able to automatically shut down during utility outage. The inverter can detect the presence of a blackout and shuts down automatically to prevent the energy it produces from harming any line workers who

are sent to fix the power grid. Grid-tie inverters that are available in the market today take advantage of a number of different technologies. They may use a variety of transformers, as the newer-higher frequency or the conventional low-frequency ones or, even, no transformer. Especially in the case of the high-frequency transformers, it is important to point out that they employ a computerized multi-step process which involves first converting the power to high-frequency AC, then back to DC and then to the final desired AC output voltage, instead of converting current directly to 120 or 240 volts AC [48].

- **Battery backup inverters:** Battery backup inverters are a special kind of inverters, which are designed to draw energy from a battery. They use an onboard charger to manage the battery charge and export excess energy to the utility grid. This type of inverters is capable of supplying AC energy to selected loads during a utility outage and are required to have anti-islanding protection, just like the grid-tied ones.

Since the scope of our projects at the moment is focused on maximizing the feed-in, the most adequate type of inverter would be a grid-tied one. It is especially important to pick an inverter suited to the power demand of each specific building, to make sure that the load will be suitable to the device of our choice. As a general rule, the power of the inverter should follow the equation:

$$\text{Power of inverter} = \text{power requirement} / \text{power factor}$$

Equation 22: *Power of inverter*

To be on the safe side of the calculations, from now on we will assume a power factor of 0.7.

6. RESULTS

6.1 Mask R-CNN Accuracy

The model's performance under the first training set was poor with the the accuracy of the generated ROI's and the final boundary boxes was below average. Thus, the applied masks failed to capsule the target pixels which corresponded to a rooftop. Two distinct outputs that demonstrate the model's inaccuracy are showcased in figures 18 and 19. In the first case , the model managed to correctly classify only a portion of the building, which is highlighted with a red color mask, while a parking area along with nearby roads are falsely classified as rooftops. On the other hand, in Figure 19 the model's precision is significantly higher since it manages to correctly classify the main building in the center of the image. This is not the case however, in terms of mask accuracy. Even though the mask covers most of rooftop's surface, it falsely includes numerous portions of surroundings. Let alone, a major part of a neighboring road that is incorrectly classified as a building as well.



Figures 13a, 13b: Demonstration of two distinct cases of model's misclassifications under the first training set

Under the second dataset however, model accuracy was significantly higher. The boundary box classification is now more precise while the generated masks describe the identified rooftops in a more valid manner.

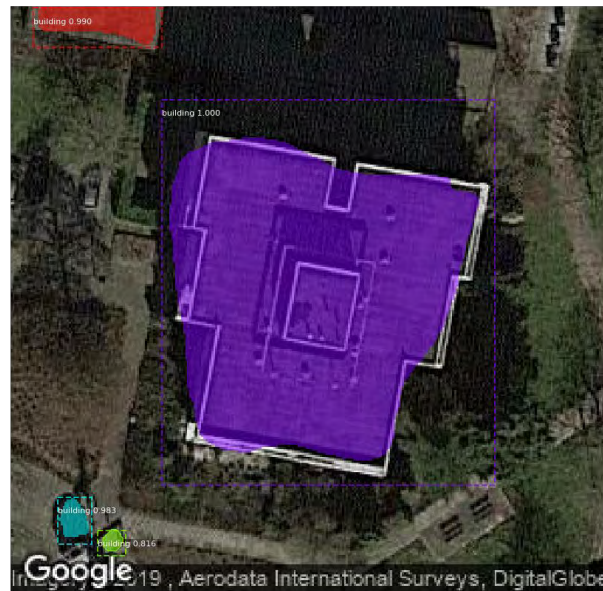


Figure 14: *Model performance under the second dataset.*

The results of this comparison are presented in Table 4. The model seems to be way more efficient in identifying rooftops belonging to commercial buildings like large storehouses, factories, etc. The model's accuracy further increases when the surrounding patterns correspond to rural area scenery, something that also applies to residential buildings. The reason why this inconsistency in terms of accuracy occurs has to do with the distinct variation between textures in countryside locations. The wider spaces, the lack of shading from larger structures and the home's architecture in general, seem to benefit the model prediction precision. On the other hand, in urban areas, the distance between buildings is limited making the discrimination even harder. Moreover, in Amsterdam's case, many paved roads happen to have similar textures to many tile roofs, an occasion which the model struggle to distinguish. Lastly, the lower accuracy rates within city limits are also a result of Amsterdam's distinct architecture and the inability of the model to generalize in these instances. A visualization of model's accuracy is given in figures 21a and b.

Accuracy results in four different scenarios:

	Buildings within City Limits	Countryside Buildings	Overall
Commercial Buildings	0.7911	0.8539	0.8225
Residential Buildings	0.7094	0.7632	0.7363
All Buildings	0.7502	0.8086	0.7794

Table 4: Accuracy results in four different scenarios. The model is more efficient in predicting commercial buildings located in rural areas.

Demonstration of the model’s performance in the identification of a large storehouse:

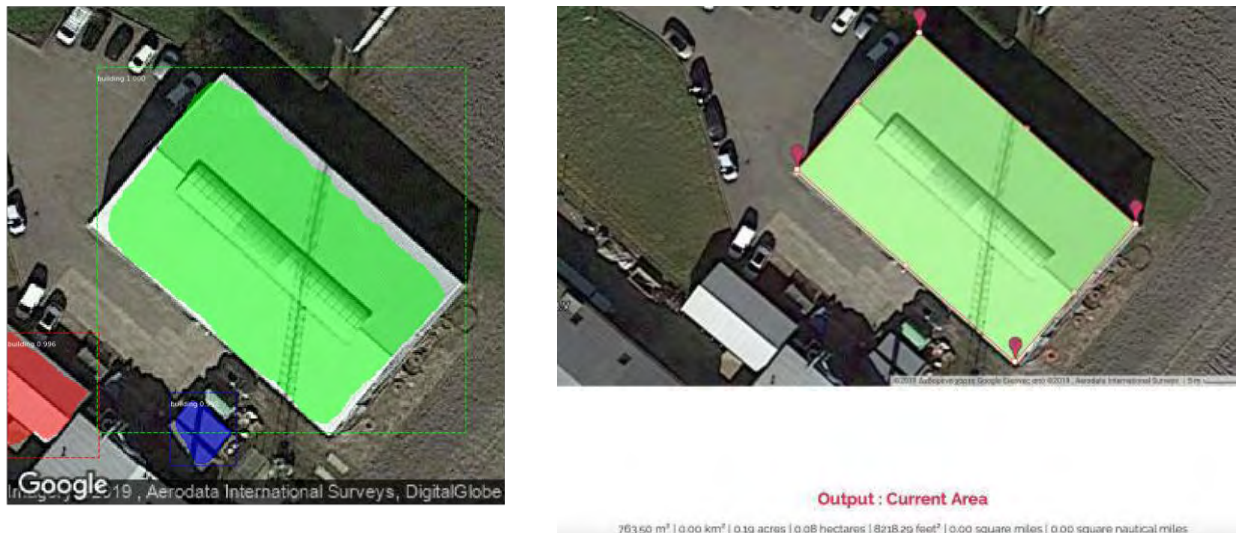


Figure 15: Demonstration of the model’s performance in the identification of a large storehouse. In this case, the size of the mask corresponds to 715.19 m² while the external tool measurement is 763.50 m² leading to 48.31 m² error. The accuracy in this instance is 93%.

Cases of Misclassification

During the evaluation process, a few frequently occurring cases of misclassification were noticed. The first and most severe one, is correlated mostly with small residential buildings under shading, something that preserves the continuity of their surrounding environment. In cases like these, as the one demonstrated in figures 22a and 22b, due to texture similarities,

the model assumes that all the similar surfaces, consist of an entire building and generates the mask along with the boundary box accordingly. The second and third instances of misclassification share many similarities. These structures are parking lots and football fields, along with basketball and tennis courts. In both occasions, the presence of vivid lines across the structure's surfaces is mistaken to be considered as a rooftop by the model. This is also the case rectangular structures in general with intense surrounding objects, like yards, which frequently tend to lead in false classifications.

A case of misclassification:



Figure 16a, 16b: *A case of misclassification. The main causes of this issue are continuity in textures and colors along with the absence of vivid segregating objects.*

6.2 Energy Yield

After examining the efficiency of our study regarding the rooftop extraction, it is now important to do the same for the annual energy yield calculations. To do so, we decided to use a website mentioned in “Literature Review”, Dutch PV Portal 2.0. The reasoning behind this choice is primarily the fact that this tool is specifically geared towards the Netherlands and uses exceptionally accurate data for the modeling, in collaboration with the Royal Netherlands Meteorological Institute. TU Delft’s Photovoltaic Materials and Devices

(PVMD) group closely monitor the forecasts' accuracy, ensuring that the output will be as realistic as possible.

In order to verify the annual energy yield calculations, we opted to test out two different cases, with different locations, orientation, solar panel type and compare them on a basis of 10 m² surface area. In the first case, the annual energy yield of a rooftop mounted polycrystalline silicon system located in Eindhoven, with a tilt of 27° and azimuth of 130° is calculated at 1.3 MWh by the Portal and at 1.397 MWh by our model, which is quite accurate. On the second case, a solar park with monocrystalline silicon panels located in northern Amsterdam, with a tilt of 60° and azimuth of 95° yields 679.64 kWh in a year according to the Portal, while our model calculates an output of 798.543 kWh for the same time period. These are some examples of the tests we conducted to determine the accuracy and efficiency of our forecasting, which is measured at an average of 87.32%.

7. CASE STUDY: RESIDENTIAL BUILDING IN HOOFDORP

As a case study, we decided to simulate the solar rooftop installation on a medium-sized, residential, south-oriented building, which is quite a common occurrence. The building we chose is situated in Hoofddorp and is part of an extended neighborhood with numerous similar buildings. The horizontal geographical coordinates of the building are 52.300541 longitude and 4.701127 latitude. As a first step, rooftop extraction was implemented through Mask R-CNN, as shown on the images below. On the image on the left (24a), we can see the part of the neighborhood where the building is situated, taken from the original Google Maps website, with a zoom level of 20. Subsequently, after applying the algorithm the result is depicted on the right (24b) where many buildings are identified, but we will focus on the one on the center, with the red mask.



Figures 17a, 17b: Residential building in Hoofddorp

It is quite obvious that Mask R-CNN's efficiency is affected by the factors mentioned before: it is important to have the whole building included in the selected area, while clear borders and colour contrast also play an important role. The efficiency of the algorithm is measured by comparing the calculated surface of the extracted area with the actual surface of the building in square meters (m^2). Since the output of the mask is in pixels, we have to convert it to m^2 to have a basis for comparison. Based on the formula described on the

“Methodology” section, the surface of the building equals to 101.2912 m² (12153 pixels). Consequently, we decided to use the “Google Maps Area Calculator Tool”, which is freely available on Daft Logic website, to compare our results with [43]. The area calculator tool measures the surface of the enclosed area, shown below, at 97.86 m², in Figure 26.

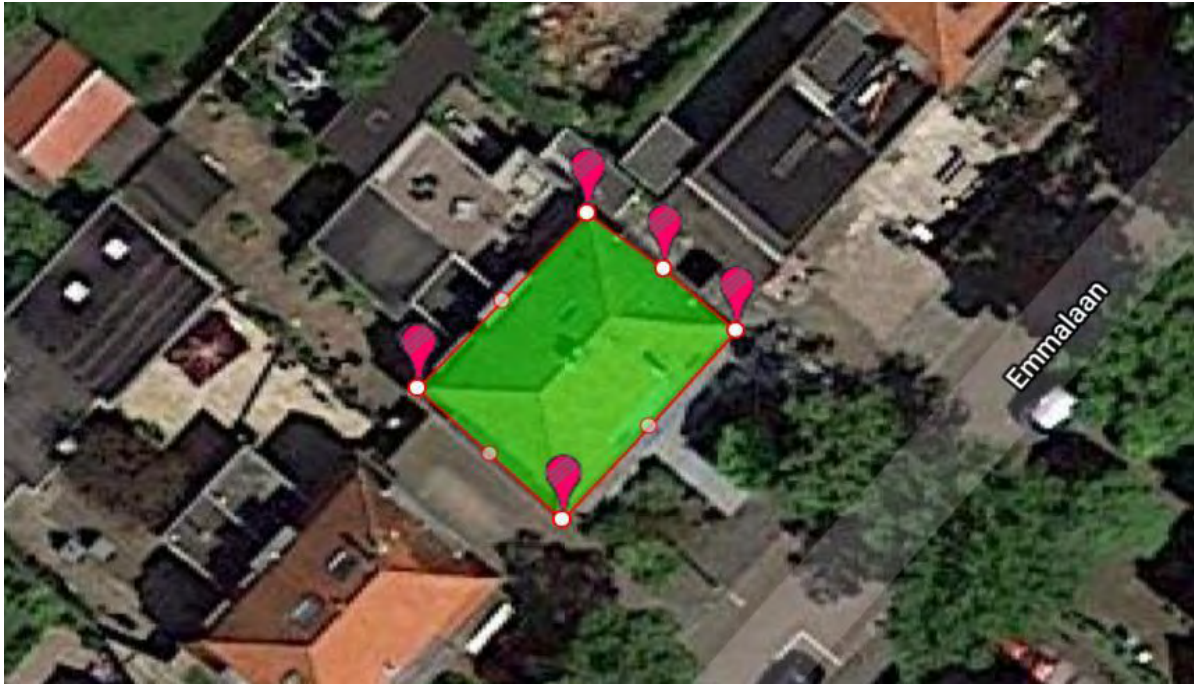


Figure 18: *Estimated rooftop area using “Google Maps Area Calculator Tool”*

As a result, the percentage of error in our calculation equals to 3.506%, which is quite precise and, thus, acceptable to use to move forward with our calculations.

Installation Specifications

As previously mentioned, the solar panel that is going to be used in this simulation is the Talesun Solar TP660P-265, which is a 265 Watt polycrystalline solar panel. The cost of each PV module amounts to 165 USD or 145.59 euros, rounded up to 150 to cover any minimal increases in the exchange rate. This was one of the top-rated, most value-for-money panels in the market in the year 2018, with the cost per Watt being really low, at 0.44 \$/Watt. It has an inbuilt system of bypass diodes (3-6) which ensure that the optimal operation of the panel is not disrupted even in the case of extreme shading. It has an open circuit voltage of $VOC = 37.9\text{ V}$, short circuit current $ISC = 9.25\text{ A}$, maximum power $PMPP = 235.7\text{ W}$, nominal

cell efficiency of $\eta = 16.3\%$, dimensions of 64.6 x 39 x 1.4 inches (1640 x 990 x 35 mm). A complete overview of the specifications can be found in appendix.

In order to implement our simulation, it is important to take into account the size of the PV modules: in our case, the Talesun TP660P-265 has dimensions of 64.6 x 39 x 1.4 inches (1640 x 990 x 35 mm), which accounts for 1.623.600 mm² or 1,623 m² per panel. Based on 101.0 m² roof, the number of panels that could be installed could vary between 55 and 61, depending on the positioning and angle of the modules. Since some space is needed to be left free on the roof for the inverter, we will consider the optimum number of PV panels to be 52, just to be on the safe side with our calculations. As a result, our system will have an installed power of 13780 kW. Based on this number, the total cost of the modules comes up to 8580 USD or 7560.68 euros, not taking into account any installation costs that might occur.

The last thing that should be considered when researching the economic viability of the project is the type and the cost of the inverter. In table 5 below, we can see the power demands of a typical dutch household nowadays. Even though the sum comes up to 15 kW, we will assume that no more than 10 kW of power are required, since for example the tumble dryer and the washing machine won't be running at the same time.

Typical power usage of household appliances:

Type of appliance	Capacity (W)
Combi fridge-freezer A+	150-200
Dishwasher	1200c
Coffee Machine	500-1000
Cooker hood	70-150
Microwave oven	1000-1500
Conventional electric oven	2000-2500
LED TV x2	20-60
Low-energy light bulbs x25	12
Game console	20-180
Tumble dryer C	2500-3000
Washing Machine A+++	2500-3000
Iron	750-1100
Vacuum cleaner	650-800
Computer with flat screen	70-80
Mobile phone charger x4	5
Hairdryer	300-600
Electric shaver	8-12
Back-up heating appliance	1000-2000
Sum	15345

Table 5: Typical power usage of household appliances

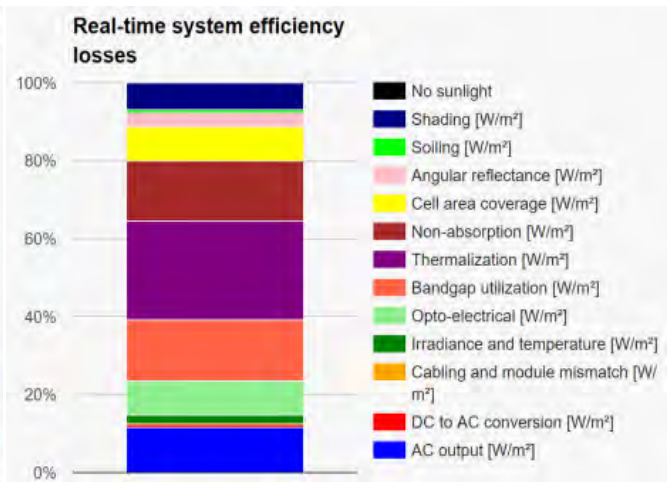
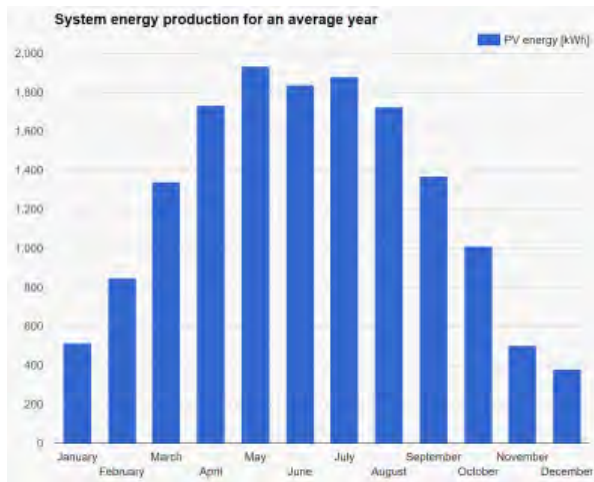
As discussed in the sections above, there are many available options when choosing an inverter, but we opted for the StorEdge SE-5000 RWS, which is a model specifically designed for the Netherlands, Austria, Germany, Switzerland and Belgium. SolarEdge is a well-known and established company in the field of PV installations and offers a guarantee of 12 years for its products, making it a very reliable option. Two of these inverters are going to be used in the installation, which will allow for 10000 W of AC Power output. This inverter provides the user with some interesting features, like the ability to remotely access and change all settings in the device, which is connected to the network, through a simple app. In addition, the app gives a lot of insight on data generated by the inverter, such as PV production and self-consumption statistics, built-in monitoring of battery status and remaining power status. These assets will be proven especially useful in the future with the addition of a battery in the system, since the feed-in prices will continuously drop and the focus will be put on maximizing self-consumption. The price of each device is 488 USD or 429.53 euro, so the total cost of them equals to 859.06 euro. As a result, the total cost of the materials for the installation is 8419.74 euro, rounded up to 9200 to include cables and rooftop installation materials (mounts, etc.).

Now, there are two different cases to go from here, depending on the user's choice. Firstly, there is the option of the manual, independent installation, with some help from an electrician to finalize the connection to the grid. The second option is to hire a specialized company to professionally install all needed components, ensure connection to the grid and take care of all maintenance. We are going to consider the first case, where the cost can be rounded up to 10000 euros, including expenses for an electrician to help with the most challenging parts of the installation. Furthermore, regarding the maintenance costs of the system, 250 euros is a normal amount for this kind of installation, inflated by 2% every passing year [49].

PV system simulation

In order to better simulate the solar yield of the Hoofddorp building installation, we used the PvLib library for python. Firstly, we ran numerous simulations with different values for the panel tilt, ending up with 48° as a best case. The azimuth is set at 157.5° , since the house is oriented towards south-east. Historical weather and irradiation data were used to calculate the losses of the system annually, according to the equations in “Methodology” section. The

distribution of the annual solar energy production is depicted on the left image (Graph 11a), while the percentages of the system's efficiency losses on the right (Graph 11b).



Graph 10a: System energy production for an average year

Graph 10b: real-time system efficiency losses

Our calculations regarding the economic feasibility and viability of the project are presented in Table 6 below, where we simulate the results of the installation during the next 10 years.

PV installation case study:

PV Installation Case Study:											
	Year 0	Year 1	Year 2	Year 3	Year 4	Year 5	Year 6	Year 7	Year 8	Year 9	Year 10
Time Period	2019	2020	2021	2022	2023	2024	2025	2026	2027	2028	2029
Installed Power (Wp)	13780										
Yearly production after losses (kWh)	15,821	15710.253	15600.28	15491.08	15382.64	15274.96	15168.04	15061.86	14956.43	14851.73	14747.77
Panel Efficiency (%)	16.20%										
Yearly Production Decrease (%)	0.70%										
Financial Calculations											
Energy price (net-metering) (€)	0.17	0.18	0.18	0.19	0.19	0.2	0.2	0.21	0.22	0.22	0.23
Energy price yearly increase rate (%)	3%										
Net-metering percentage (%)	100%	70%	60%	60%	55%	50%	40%	35%	25%	20%	15%
Feed-In tariff (€)	0	0.12	0.11	0.1	0.1	0.09	0.08	0.07	0.05	0.03	0.02
Costs											
Investments (€)	-10000										
Fixed costs (€)	-250	-255	-260.1	-265.3	-270.61	-276.02	-281.54	-287.17	-292.91	-298.77	-304.75
Inflation (%)	2%										
Earnings											
Yearly Gross Earnings (€)	2689.57	1925.64	1688.18	1726.65	1618.84	1505.21	1231.63	1102.23	805.26	658.88	505.42
Accumulated Gross Earnings (€)	2689.57	4615.21	6303.39	8030.04	9648.88	11154.09	12385.71	13487.95	14293.21	14952.09	15457.51
Accumulated Cash Flow (€)	-8524.43	-6598.79	-4910.61	-3183.96	-1565.12	-59.91	1171.71	2273.95	3079.21	3738.09	4243.51
ROI	0.185	18.50%									

Table 6: PV installation case study

Looking at this table, it is quite apparent that the system is profitable, with a Return Of Investment (ROI) of 18.5%. Return on investment, or ROI, is the ratio of a profit or loss made in a fiscal year expressed in terms of an investment and shown as a percentage of

increase or decrease in the value of the investment during the year in question. It is represented by the following equation:

$$ROI = (Return - Investment)/Investment$$

Equation 23: *ROI calculation*

It is important to point out that with the new scheme, SDE++, in order for a project to qualify for the subsidy, it should not reach the break-even point before its 6th year. As our project is supposed to reach its break-even point on year 6, it fulfills the criteria to receive the SDE++ subsidy and benefit from favorable feed-in tariffs. As the subsidy critically decreases throughout the years it would be interesting to examine as a future project the integration of a battery in the system. This move would drastically increase self-consumption, which is the main goal in the future since feed-in will become obsolete and non-profitable.

8. CONCLUSIONS AND FUTURE PROSPECTS

In this study, a computer vision based research was conducted to implement a rooftop detector able to estimate rooftop's acreage and then, using pvlb Python's toolkit, to estimate the energy output of a potential PV installation. Later on, the developed methodology was applied in a case study focusing on a medium-sized residential building in Hoofddorp, Amsterdam. The aim of this case study was to provide a tailored PV installation to the energy requirements of the aforementioned residence, whilst creating an analytical investment report based on the current legislation. Namely our model was able to produce a calculation of rooftop's area with a percentage of error equals to 3.506%. Using 52 Talesun Solar TP660P-265 PV modules and two StorEdge SE-5000 RWS inverters, it is estimated that this project will reach break-even point in year 6 and have a ROI of 18.5% against a starting cost of 9200 euros. The methods described in the sections above can be used in numerous different cases and are not limited on small or big buildings, urban or rural areas, shaded or not.

Finally, this research allows room for potential improvement. The detector's accuracy could be increased and further individualized to the Netherlands, especially in detection within the city-scape. Furthermore, the addition of batteries and energy management system in case studies would frame the broader picture of the future, which is centered around the maximization of self-consumption. Since the SDE++ pushes Dutch PV energy producers in this direction, aiming to minimize feeding-in the grid, a research focused purely on the impact of these components should follow this one, to counteract the problem as a whole. Last but not least, based on this thesis work, the ultimate goal would be to implement a web-based application allowing the process discussed in previous chapters to be autonomous and personalized, intending to assist energy consumers who are willing to invest in renewable energy sources but hesitate to take the first step.

REFERENCES

- [1] Höök, M. (2019). *Depletion and Decline Curve Analysis in Crude Oil Production*. 1st ed. [ebook] Uppsala. Available at: <http://www.diva-portal.org/smash/get/diva2:338111/FULLTEXT01> [Accessed 27 Feb. 2019].
- [2] Ott, A. (2010). *Benzene pollution - a health risk in Gulf BP Oil drilling disaster - La Leva di Archimede (ENG)*. [online] Laleva.org. Available at: http://www.laleva.org/eng/2010/05/benzene_pollution_a_health_risk_in_gulf_bp_oil_drilling_disaster.html [Accessed 27 Feb. 2019].
- [3] Grin, J., Rotmans, J. and Schot, J. (2010). *Transitions to sustainable development*. New York, NY: Routledge.
- [4] Reuters (2019). *Dutch will miss 2020 green energy, climate targets: report*. [online] U.S. Available at: <https://www.reuters.com/article/us-netherlands-climatechange/dutch-will-miss-2020-green-energy-climate-targets-report-idUSKBN1CO2EV> [Accessed 27 Feb. 2019].
- [5] *Solar Energy Perspectives: Executive summary*. (2011). Paris: Organisation for Economic Cooperation and Development (OECD).
- [6] Solargis.com. (2019). *Solar resource maps of Netherlands*. [online] Available at: <https://solargis.com/maps-and-gis-data/download/netherlands/> [Accessed 28 Feb. 2019].
- [7] Szeliski, R. (2011). *Computer vision: Algorithms and Applications*. London: Springer Science & Business Media, pp.10-16.
- [8] Google.com. (2019). *Project Sunroof - Solar Calculator*. [online] Available at: <https://www.google.com/get/sunroof#p=0> [Accessed 8 Apr. 2019].

- [9] Karpath, A. (n.d.). CS231n Convolutional Neural Networks for Visual Recognition. [online] Cs231n.github.io. Available at: <http://cs231n.github.io/convolutional-networks/#conv> [Accessed 6 Apr. 2018].
- [10] TU Delft. (n.d.). *Dutch PV Portal*. [online] Available at: <https://www.tudelft.nl/ewi/over-de-faculteit/afdelingen/electrical-sustainable-energy/photovoltaic-materials-and-devices/dutch-pv-portal/> [Accessed 28 Feb. 2019].
- [11] Energievergelijk. (n.d.). *Energy suppliers in The Netherlands – Energievergelijk*. [online] Available at: <https://www.energievergelijk.nl/english/energy-suppliers> [Accessed 8 Nov. 2018].
- [12] energievergelijken.nl. (n.d.). *About energy in The Netherlands / What you need to know*. [online] Available at: <https://www.energievergelijken.nl/en/about-energy-in-the-netherlands> [Accessed 8 Nov. 2018].
- [13] Foxon, T. (2008). Managing the transition to renewable energy: theory and practice from local, regional and macro perspectives. *Environmental Sciences*, 5(4), pp.286-288.
- [14] Piret Tõnurist, David den Besten, Pieter Vandeven, Xinhui Yu, Dalia Paplaityte. 2015. “Market Liberalization and Innovation in the Energy Sector: The Case of Belgium and the Netherlands.” *Administrative Culture* 16 (2), 83 -116
- [15] Statista. (n.d.). *Netherlands: electricity DSO market share 2016 / Statistic*. [online] Available at: <https://www.statista.com/statistics/878534/electricity-dso-market-share-in-the-netherlands/> [Accessed 8 Nov. 2018].
- [16] Rvo.nl. (n.d.). *Stimulering Duurzame Energieproductie / RVO.nl*. [online] Available at: <https://www.rvo.nl/subsidies-regelingen/stimulering-duurzame-energieproductie> [Accessed 10 Jan. 2019].
- [17] Wu, J. (2017). Introduction to Convolutional Neural Networks.

- [18] Doitpoms.ac.uk. (n.d.). *DoITPoMS - TLP Library Tensors in Materials Science - What is a Tensor?*. [online] Available at: https://www.doitpoms.ac.uk/tlplib/tensors/what_is_tensor.php [Accessed 5 Apr. 2018].
- [19] Brownlee, J. (n.d.). *What is the Difference Between a Batch and an Epoch in a Neural Network?*. [online] Machine Learning Mastery. Available at: <https://machinelearningmastery.com/difference-between-a-batch-and-an-epoch/> [Accessed 12 Jan. 2019].
- [20] [superdatascience.com](https://www.superdatascience.com) (n.d.). *SuperDataScience*. [online] Available at: <https://www.superdatascience.com/convolutional-neural-networks-cnn-step-1b-relu-layer/> [Accessed 6 Apr. 2018].
- [21] Karpath, A. (n.d.). *CS231n Convolutional Neural Networks for Visual Recognition*. [online] Cs231n.github.io. Available at: <http://cs231n.github.io/convolutional-networks/#conv> [Accessed 6 Apr. 2018].
- [22] Hui, J. (2018). *What do we learn from region based object detectors (Faster R-CNN, R-FCN, FPN)?*. [online] Medium. Available at: https://medium.com/@jonathan_hui/what-do-we-learn-from-region-based-object-detectors-faster-r-cnn-r-fcn-fpn-7e354377a7c9 [Accessed 23 Jun. 2018].
- [23] Evaluation of Pooling Operations in Convolutional Architectures for Object Recognition
- [24] [superdatascience.com](https://www.superdatascience.com). (n.d.). *SuperDataScience*. [online] Available at: <https://www.superdatascience.com/convolutional-neural-networks-cnn-step-2-max-pooling/> [Accessed 6 Apr. 2019]
- [25] Girshick, R. (2015). Fast R-CNN. 2015 IEEE International Conference on Computer Vision (ICCV).
- [26] Grel, T. (2017). *Region of interest pooling explained*. [online] deepsense.ai.

Available at: <https://deepsense.ai/region-of-interest-pooling-explained/> [Accessed 29 Jun. 2018].

[27] Ren, S., He, K., Girshick, R. and Sun, J. (2015). Faster R-CNN: Towards Real-Time Object Detection with Region Proposal Networks. *IEEE Transactions on Pattern Analysis and Machine Intelligence* 39(6).

[28] Parthasarathy, D. (2017). *A Brief History of CNNs in Image Segmentation: From R-CNN to Mask R-CNN*. [online] Athelas. Available at: <https://blog.athelas.com/a-brief-history-of-cnns-in-image-segmentation-from-r-cnn-to-mask-r-cnn-34ea83205de4> [Accessed 12 Jan. 2019].

[29] Tsoros, S. and Ioannis, T. (2010). ΑΝΑΠΤΥΞΗ ΟΙΚΟΝΟΜΟΤΕΧΝΙΚΗΣ ΜΕΘΟΔΟΛΟΓΙΑΣ ΓΙΑ ΤΗΝ ΕΚΜΕΤΑΛΛΕΥΣΗ ΦΩΤΟΒΟΛΤΑΪΚΩΝ ΣΤΟΙΧΕΙΩΝ (Φ/Β) (Παράδειγμα πρότυπης ενεργειακής μελέτης τοποθέτησης φ/β, διασυνδεδεμένων με το δίκτυο της ΔΕΗ σε στέγαστρα αποβάθρων σταθμών ηλεκτρικού αστικού σιδηροδρόμου).

[30] Photovoltaic-software.com. (2019). *How to calculate output energy of PV solar systems?*. [online] Available at: <https://photovoltaic-software.com/principle-ressources/how-calculate-solar-energy-power-pv-systems> [Accessed 3 Dec. 2018].

[31] Reno, M., Hansen, C. and Stein, J. (2012). Global Horizontal Irradiance Clear Sky Models: Implementation and Analysis.

[32] China Office. (2014). *Difference Solar Radiation and Solar Insolation explained - Sinovoltaics - Your Solar Supply Network*. [online] Sinovoltaics - Your Solar Supply Network. Available at: <https://sinovoltaics.com/learning-center/basics/solar-radiation-solar-insolation/> [Accessed 6 Dec. 2018].

[33] Pvpmmc.sandia.gov. (n.d.). *PV Performance Modeling Collaborative / Extraterrestrial radiation*. [online] Available at: <https://pvpmmc.sandia.gov/modeling-steps/1-weather-design-inputs/irradiance-and-insolation-2/extraterrestrial-radiation/> [Accessed 5 Dec. 2018].







- [34] Holiday-weather.com. (n.d.). *Amsterdam, Netherlands Average Annual Weather - Holiday Weather*. [online] Available at: <https://www.holiday-weather.com/amsterdam/averages/> [Accessed 27 Feb. 2019].
- [35] Ineichen, P. and Perez, R. (2001). A new air mass independent formulation for the Linke turbidity coefficient.
- [36] Broadfoot, C. (2011). *Google Groups*. [online] Groups.google.com. Available at: <https://groups.google.com/forum/#!msg/google-maps-js-api-v3/hDRO4oHVSeM/osOYQYXg2oUJ> [Accessed 22 Aug. 2018].
- [37] Wiki.openstreetmap.org. (n.d.). *Zoom levels - OpenStreetMap Wiki*. [online] Available at: https://wiki.openstreetmap.org/wiki/Zoom_levels [Accessed 8 Feb. 2019].
- [38] Abdulla, W. (2017). Mask R-CNN for object detection and instance segmentation on Keras and TensorFlow. *GitHub repository*.
- [39] Mohanty, S. (2018). CrowdAI Mapping Challenge 2018 : Baseline with Mask R-CNN.
- [40] Lin, T., Maire, M., Belongie, S., Bourdev, L., Girshick, R., Hays, J., Perona, P., Ramanan, D., Zitnick, C. and Dollár, P. (2015). Microsoft COCO: Common Objects in Context.
- [41] CrowdAI. (2019). *CrowdAI Mapping Challenge*. [online] Available at: https://www.crowdai.org/challenges/mapping-challenge/dataset_files [Accessed 20 Jul. 2018].
- [43] Holmgren, W., Hansen, C. and Mikofski, M. (2018). pvlib python: a python package for modeling solar energy systems. *The Journal of Open Source Software*.

- [44] Pvlib-python.readthedocs.io. (n.d.). *pvlib-python — pvlib-python 0.6.1+0.gd621327.dirty documentation*. [online] Available at: <https://pvlib-python.readthedocs.io/en/latest/> [Accessed 6 Dec. 2018].
- [45] Reda, I. and Andreas, A. (2008). Solar Position Algorithm for Solar Radiation Applications. *NREL: National Renewable Energy Laboratory*.
- [46] Kołodziej, A. (2015). *Staebler-Wronski effect in amorphous silicon and its alloys*. [online] Infona.pl. Available at: <https://www.infona.pl/resource/bwmeta1.element.baztech-article-BWA1-0005-0076> [Accessed 10 Feb. 2019].
- [47] Saleh, M., Esa, Y., Mhandi, Y., Brandauer, W., Mohamed, A. (2016). "Design and implementation of CCNY DC microgrid testbed". *2016 IEEE Industry Applications Society Annual Meeting*: 1–7. [doi:10.1109/IAS.2016.7731870](https://doi.org/10.1109/IAS.2016.7731870).
- [48] Solar Energy International (2004). *Photovoltaics: Design and Installation Manual*. New Society Publishers.
- [49] theOECD. (n.d.). *Prices - Inflation forecast - OECD Data*. [online] Available at: <https://data.oecd.org/price/inflation-forecast.htm> [Accessed 16 Feb. 2019].

APPENDIX



KEY FEATURES

- 
Maximize limited space
 Maximum power output 275W
- 
Excellent Anti-PID performance
 2 times of industry standard Anti-PID test by TUV Rheinland
- 
Highly reliable due to stringent quality control
 In-house testing goes well beyond certification requirements
- 
Certified to withstand the most challenging environmental conditions
 2400 Pa wind load · 5400 Pa snow load · 25 mm hail stones at 82 km/h
- 
IP68 junction box
 The highest waterproof level
- 
Lower temperature coefficients
 Enhance power generation

ABOUT TALESUN SOLAR

TALESUN Solar is one of the world's largest integrated clean energy providers with 4 GW cell and 5 GW module production capacity globally. Its standard and high-efficiency product offerings are among the most powerful and cost-effective in the industry. Talesun Solar is committed to provide customers with customized; systematized and trustworthy turnkey solutions. Till now, Talesun Solar has accumulatively shipped more than 10 GW modules globally.

SYSTEM & PRODUCT CERTIFICATES

- IEC 61215 / IEC 61730 / UL 1703
- ISO 9001 : 2008 Quality Management System
- ISO 14001 : 2004 Environment Mangement System
- OHSAS 18001 : 2007 Occupational Health and Safety Management System

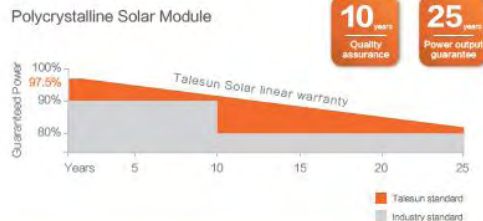


QUALITY WARRANTY

TALESUN guarantees that defects will not appear in materials and workmanship defined by IEC61215, IEC61730 or UL1703 under normal installation, use and maintenance as specified in Talesun's installation manual for 10 years from the warranty starting date.



PERFORMANCE WARRANTY



TALESUN



Web: www.talesun.com
 Tel: + 86 400 885 1008
 Add: No.1 Talesun Road, Shajiang, Changshu, P.R. China

ELECTRICAL PARAMETERS

Performance at STC (Power Tolerance 0 – +3%)

Maximum Power (P _{max} /W)	265	270	275
Operating Voltage (V _{mpp} /V)	31.0	31.3	31.7
Operating Current (I _{mpp} /A)	8.56	8.63	8.69
Open-Circuit Voltage (V _{oc} /V)	38.2	38.5	38.7
Short-Circuit Current (I _{sc} /A)	9.04	9.09	9.17
Module Efficiency η _m (%)	16.2	16.5	16.8

Performance at NOCT

Maximum Power (P _{max} /W)	196	199	203
Operating Voltage (V _{mpp} /V)	28.7	28.9	29.2
Operating Current (I _{mpp} /A)	6.83	6.90	6.97
Open-Circuit Voltage (V _{oc} /V)	35.2	35.5	35.7
Short-Circuit Current (I _{sc} /A)	7.32	7.36	7.42

STC: Irradiance 1000W/m², Cell Temperature 25° C, Air Mass AM1.5. NOCT: Irradiance at 800W/m², Ambient Temperature 20° C, Wind Speed 1m/s

MECHANICAL SPECIFICATION

Cell Type	Poly
Cell Dimensions	156.75*156.75mm(6inch)
Cell Arrangement	60(6*10)
Weight	18.5kg(48.5lbs)
Module Dimensions	1650*992*35mm(64.96*39.06*1.38inch)
Cable Length	900mm(47.24inch)
Cable Cross Section Size	4mm ² (0.008sq.in)
Front Glass	3.2mm High Transmission, Tempered Glass
No. of Bypass Diodes	3/6
Packing Configuration (1)	30pcs/Pallet,840pcs/40hq
Packing Configuration (2)	30pcs+5pcs/Pallet, 910pcs/40hq
Frame	Anodized Aluminium Alloy
Junction Box	IP68

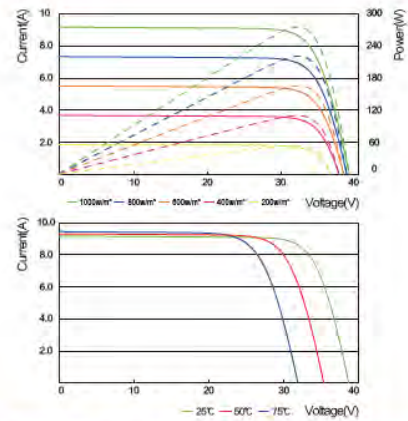
OPERATING CONDITIONS

Maximum System Voltage	1000V/DC(IEC)/1500V/DC(IEC)
Operating Temp.	-40°C~+85°C
Maximum Series Fuse	15A
Static Loading	5400Pa
Conductivity at Ground	≤ 0.1Ω
Safety Class	II
Resistance	≥ 100MΩ
Connector	MC4 Compatible

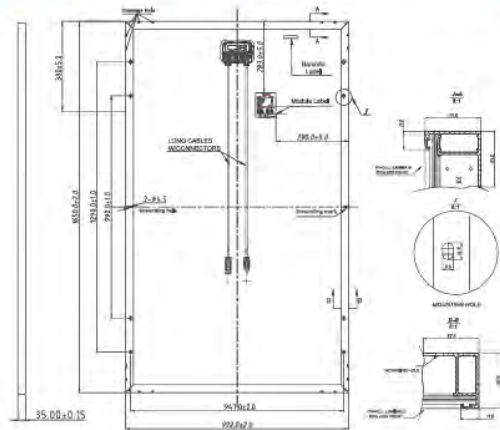
TEMPERATURE COEFFICIENT

Temperature Coefficient P _{max}	-0.40%/°C
Temperature Coefficient V _{oc}	-0.31%/°C
Temperature Coefficient I _{sc}	+0.06%/°C
NOCT	45 ± 2°C

I-V CURVE



TECHNICAL DRAWINGS



The specification and key features described in this datasheet may deviate slightly and are not guaranteed. Due to ongoing innovation, R&D enhancement, Suncoo Talesun Solar Technologies Co., Ltd. reserves the right to make any adjustment to the information described herein at any time without notice. Please always obtain the most recent version of the datasheet which shall be duly incorporated into the binding contract made by the parties governing all transactions related to the purchase and sale of the products described herein. 3018100EN

TALESUN

StorEdge Single Phase Inverter

for DACH, Belgium & The Netherlands

SE5000-RWS



STOREDGE™

Ideal for battery storage and backup power

- Supports StorEdge Solution Applications - reduce electric bills with maximised self-consumption and profile programming
- Provides Backup Power - StorEdge Inverter includes the hardware required for automatically supplying power to backed-up loads in the event of grid outages
- Simple Design and Installation - single inverter for managing PV production, battery storage and backup power
- Enhanced Safety - designed to eliminate high voltage during installation, maintenance or firefighting
- Full Visibility - built-in monitoring of battery status, PV production, remaining backup power, and self-consumption data
- Easy Maintenance - remote access to inverter software

solaredge.com

solaredge

/ StorEdge Single Phase Inverter

for DACH, Belgium & The Netherlands

SE5000-RWS⁽¹⁾

SE5000-RWS		
OUTPUT - AC (LOADS/GRID)		
Rated AC Power Output	5000 ⁽²⁾	VA
Max AC Power Output	5000 ⁽²⁾	VA
AC Output Voltage (Nominal), L-N ⁽³⁾	220 / 230	Vac
AC Output Voltage Range, L-N	184 - 264.5	Vac
AC Frequency	50 / 60 ± 5	Hz
Maximum Continuous Output Current	25	A
Residual Current Detector / Residual Current Step Detector	300 / 30	mA
Utility Monitoring, Islanding Protection, Country Configurable Thresholds	Yes	
Charge Battery from AC (if Allowed)	Yes	
THD	< 3	%
OUTPUT - AC (BACKUP POWER)⁽⁴⁾		
Rated AC Power Output	5000	VA
Max AC Power Output - Surge (for 10 seconds)	7000	VA
AC Output Voltage (Nominal)	220 / 230	Vac
AC Output Voltage Range	184 - 264.5	Vac
AC Frequency	50 / 60 ± 5	Hz
Maximum Continuous Output Current	22	A
AC Breaker	Yes	
THD	< 5	%
Power factor with rated power	0.2 leading to 0.2 lagging	
Automatic switchover time	< 2	sec
INPUT - DC (PV AND BATTERY)		
Transformer-less, Ungrounded	Yes	
Max Input Voltage	500	Vdc
Nom DC Input Voltage	400	Vdc
Reverse-Polarity Protection	Yes	
Ground-Fault Isolation Detection	600kΩ Sensitivity	
Maximum Inverter Efficiency	97.6	%
European Weighted Efficiency	97.4	%
INPUT - DC (PV)		
Maximum DC Power (STC)	6750	W
Max Input Current	19.5	Adc
2-pole Disconnection	Yes	
INPUT - DC (BATTERY)		
Supported Battery Types	LG Chem RESU7H LG Chem RESU10H ⁽⁵⁾	
Number of Batteries per Inverter	1	
Continuous Power	LG Chem RESU7H: 3500, LG Chem RESU10H: 5000	W
Peak Power	LG Chem RESU7H: 5000, LG Chem RESU10H: 7000	W
Max Input Current	17.5	Adc
2-pole Disconnection	Yes	
DC Fuses on Plus and Minus	25A (field replaceable)	

⁽¹⁾ An external disconnection unit is required

⁽²⁾ Limited to 4600VA when inverter is set to Germany

⁽³⁾ The StorEdge Inverter must be connected Line to Neutral (and not Line to Line)

⁽⁴⁾ Not designed for standalone applications and requires AC for commissioning

⁽⁵⁾ LG Chem RESU10H battery can be connected only to inverters with part number: SE5000-RWS2XXXXX

/ StorEdge Single Phase Inverter

for DACH, Belgium & The Netherlands

SE5000-RWS

ADDITIONAL FEATURES		
Supported Communication Interfaces	RS485 for battery, RS485, Ethernet, ZigBee (optional), Wi-Fi (optional)	
Battery Power Supply	Yes, 12V / 53W	
Integrated AC, DC and Communication Connection Unit	Yes	
AC Disconnect	Yes	
Manual Inverter Bypass Switch	Yes	
DC Voltage Rapid Shutdown (PV and Battery)	Yes, according VDE-AR-E 2100-712 (part7); OVE R11-1	
Backup Power Requirements	An external disconnection unit is required to ensure Neutral and/or Ground disconnection requirements in backup. The inverter is compatible with units provided by Enwitec (http://enwitec.eu). 2 types of external disconnection units are available: Single phase for Belgium and The Netherlands, and Three Phase for DACH	
STANDARD COMPLIANCE		
Safety	IEC-62103 (EN50178), IEC-62109	
Grid Connection Standards ¹⁾	VDE-AR-N-4105; VDE-AR 2510-2 ²⁾	
Emissions	IEC61000-6-2, IEC61000-6-3, IEC61000-3-11, IEC61000-3-12	
INSTALLATION SPECIFICATIONS		
AC Output (Loads/Grid) conduit size / wire cross section	9-16mm / 2-14mm ²	
AC Output (Backup) conduit size / wire cross section	9-16mm / 2-14mm ²	
DC Input (PV)	2 MC4 pairs	
DC Input (Battery)	1 MC4 pair	
Dimensions with Connection Unit (HxWxD)	962 x 315 x 184	mm
Weight with Connection Unit	26.5	kg
Cooling	Natural convection and internal fan (user replaceable)	
Noise	<50	dB(A)
Min - Max Operating Temperature	-20 to +60 ³⁾	°C
Protection Rating	IP65 - Outdoor and Indoor	

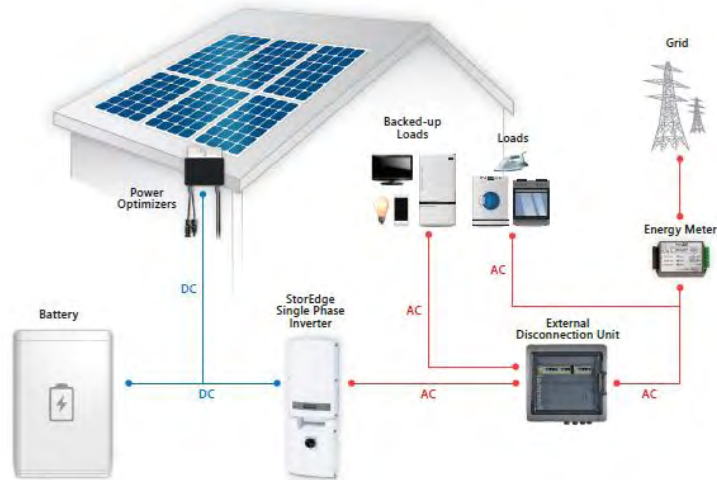
¹⁾ For all standards refer to Certifications category in Downloads page: <http://www.solaredge.com/groups/support/downloads>

²⁾ Applies in conjunction with the external disconnection unit

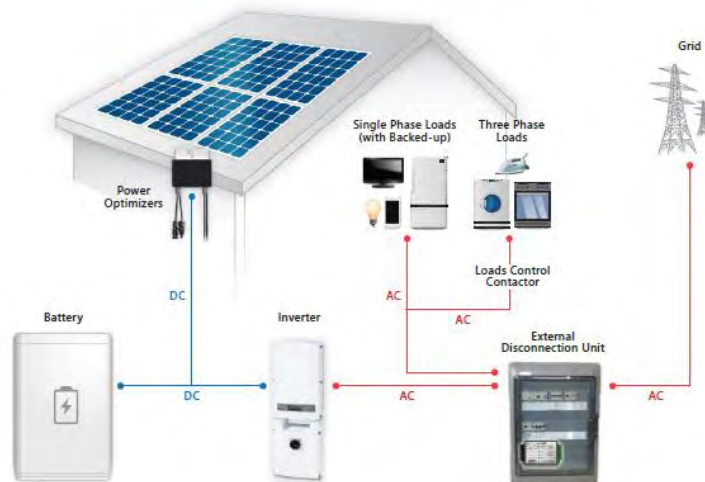
³⁾ Power derating from 50 °C

/ StorEdge Single Phase Inverter for DACH, Belgium & The Netherlands SE5000-RWS

StorEdge Solution with Backup Power and Single Phase External Disconnection Unit for Belgium and The Netherlands



StorEdge Solution with Backup Power and Three Phase External Disconnection Unit for DACH



© SolarEdge Technologies, Ltd. All rights reserved. SOLAREEDGE, the SolarEdge logo, OPTIMIZED BY SOLAREEDGE are trademarks or registered trademarks of SolarEdge Technologies, Inc. All other trademarks mentioned herein are trademarks of their respective owners. 12/2018/W01/ROW. Subject to change without notice.